The Journal of Undergraduate Research in Physics

Volume 12, Number 2
May, 1994

Published by the Physics Department of Guilford College
for
The American Institute of Physics and the Society of Physics Students

THE JOURNAL OF UNDERGRADUATE RESEARCH IN PHYSICS

This journal is devoted to research work done by undergraduate students in physics and its related fields. It is to be a vehicle for the exchange of ideas and information by undergraduate students. Information for students wishing to submit manuscripts for possible inclusion in the Journal follows.

ELIGIBILITY
The author(s) must have performed all work reported in the paper as an undergraduate student(s). The subject matter of the paper is open to any area of pure or applied physics or physics related field.

SPONSORSHIP
Each paper must be sponsored by a full-time faculty member of the department in which the research was done. A letter from the sponsor, certifying that the work was done by the author as an undergraduate and that the sponsor is willing to be acknowledged at the end of the paper, must accompany the manuscript if it is to be considered for publication.

SUBMISSION
Two copies of the manuscript, the letter from the sponsor and a telephone number or E-Mail address where the author can be reached should be sent to:

Dr. Rexford E. Adelberger, Editor
THE JOURNAL OF UNDERGRADUATE
RESEARCH IN PHYSICS
Physics Department
Guilford College
Greensboro, NC 27410

FORM
The manuscript should be typed, double spaced, on 8 1/2 x 11 inch sheets. Margins of about 1.5 inches should be left on the top, sides, and bottom of each page. Papers should be limited to fifteen pages of text in addition to an abstract (not to exceed 250 words) and appropriate drawings, pictures, and tables.

Manuscripts may be submitted on a disk that can be read by a MacIntosh™. The files must be compatible with MacWrite™, MicroSoft Word™ , PageMaker™ or WordPerfect™.

ILLUSTRATIONS
Line drawings should be made with black ink on plain white paper. Each figure or table must be on a separate sheet. Photographs must have a high gloss finish. If the submission is on a disk, the illustrations should be in PICT, TIFF or EPS format.

CAPTIONS
A brief caption should be provided for each illustration or table, but it should not be part of the figure. The captions should be listed together at the end of the manuscript

EQUATIONS
Equations should appear on separate lines, and may be written in black ink. We use EXPRESSIONIST™ to format equations in the Journal.

FOOTNOTES
Footnotes should be typed, double spaced and grouped together in sequence at the end of the manuscript.

PREPARING A MANUSCRIPT
A more detailed set of instructions for authors wishing to prepare manuscripts for publication in the Journal of Undergraduate Research in Physics can be found in Volume 8 #1 which appeared in October of 1989 or in Volume 11 #2 which appeared in May of 1993.

SUBSCRIPTION INFORMATION

The Journal is published twice each academic year, issue # 1 appearing in November and issue # 2 in May of the next year. There are two issues per volume.

TYPE OF SUBSCRIBER	PRICE PER VOLUME
Individual	$US 5.00
Institution	$US 10.00

Foreign subscribers add $US 2.00 for surface postage, $US 10.00 for air freight.

Back issues may be purchased by sending $US 15.00 per volume to the editorial office.

To receive a subscription, send your name, address, and check made out to **The Journal of Undergraduate Research in Physics (JURP)** to the editorial office:

JURP
Physics Department
Guilford College
Greensboro, NC 27410

The Journal of Undergraduate Research in Physics is sent to each member of the Society of Physics Students as part of their annual dues.

A QUANTUM MONTE CARLO STUDY OF He_nCl_2 CLUSTERS

Darin P. Diachin*
Department of Physics and Astronomy
Arizona State University
Tempe, AZ 85287-1504
received November 9, 1993

ABSTRACT

The results of variational and Green's function Monte Carlo calculations for the ground state properties of He_nCl_2 clusters are presented. Variational ground state energies are provided for n ranging from 2 to 28 as well as Green's function ground state energies for $n = 8,18$ and 28. Radial probability distributions are consistently broad in shape for all n, with He atoms showing a peak in probability at approximately 4.5Å from the Cl_2 center of mass. Angular distributions are spherical for $n>15$, which indicate that the clusters take the form of a droplet.

INTRODUCTION

Several advances have been made in recent years in the study of van der Waals clusters composed of rare gas atoms and a diatomic molecule. A wide array of such clusters have been discovered composed of rare gas species with Cl_2, Br_2, I_2, ICl and HF molecules. High resolution spectroscopy has been used to isolate vibrational and rotational excited state spectra of several of these molecules, some of which have been successfully reproduced using classical or semiclassical theoretical systems.

Laser pump probe techniques were used to obtain rotational excited state spectra for Ne_2Cl_2 and Ar_2Cl_2, which could be modeled using a rigid rotor representation. [1] In both cases, a "distorted tetrahedron" was found to produce the closest fit to the observed spectra. However, the same technique failed to reproduce experimental results for He_2Cl_2. In this case, it was postulated that no average molecular structure existed due to an unusually small separation between vibrational and rotational quantum configurations. The resulting cluster was presumed to have large fluctuations in the ground state structure. This was supported by the fact that all four rigid rotor structures that were investigated resulted in potential energies below the estimated zero point energy of the complex.

Darin is a senior at the Colorado School of Mines and is majoring in applied mathematics. He is currently developing sensor fusion software with a grant from the Colorado Advanced Software Institute. He intends to pursue his graduate work in applied mathematics or computational physics. This work was conducted under the Arizona State University Research Experience for Undergraduates in Condensed Matter Physics.

This research, as well as similar results for other floppy systems, motivated a development of a quantum mechanical model for He_2Cl_2 and He_3Cl_2. [3] The results reflected a great deal of variability in the ground state probability functions for various positional configurations. In the case of He_2Cl_2, radial distances r, as defined by Figure 1, proved to be highly probable between 3Å and 5.5Å. He-He distances ranged from 2Å to 10Å with a maximum at approximately 7Å. Angular positions, θ, had a high probability between 60° and 120°, with a maximum probability at 90°.

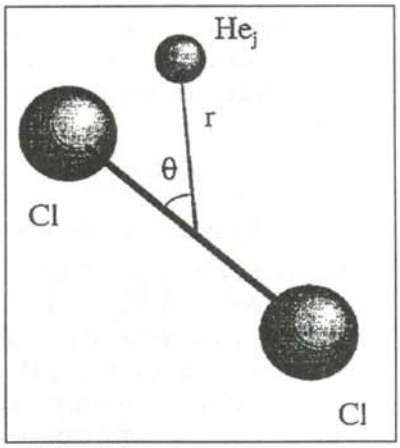

Figure 1
A model showing the two degrees of freedom studied. r is a measure of the radial distance of the helium atom to the center of mass of the chlorine molecule. θ represents the angle that the helium atom makes with respect to the axis

This work extends the computer programs used to model the He_2Cl_2 cluster to investigate the dynamics of these floppy probability distributions as the number of He atoms are increased. Tendencies of the He atoms to crystallize or remain liquid as well as the locus of the chlorine molecule within the cluster are addressed.

METHODOLOGY

The two techniques used to compute the ground state properties of the He_2Cl_2 clusters were the variational and the Green's function Monte Carlo (GFMC) methods. While both methods are deemed Monte Carlo due to their use of random variable sampling, they are two separate algorithms and require separate treatment. More details about these methods can be found elsewhere. [3,4,5,6]

Variational Monte Carlo Method

The variational method essential produces two results: an upper bound for the ground state energy of the cluster, E_o, and the distribution configurations of the atoms themselves computed from a carefully considered trial wave function, ψ_T. The first priority of this method is determining the form of the wave function suitable to approximate the actual ground state wave functions. An estimation of E_o can then be calculated by employing the Rayleigh-Ritz variational principle:

$$\langle H \rangle = E_o \leq \frac{\int \psi_T(R)\, H\, \psi_T(R)\, dR}{\int \psi_T{}^2(R)\, dR} , \qquad (1)$$

where R is a vector representing the 3N coordinates of the N particles.

The trial wave function used for this work was the Bijl-Dingle-Jastrow wave function (commonly referred to as the Jastrow wave function), which assumes that the wave function can be represented as a product of two-body correlations:

$$\psi_T(R) = \prod_{i<j} f_{ij}(\left|\vec{r}_i - \vec{r}_j\right|) , \qquad (2)$$

where $\left|\vec{r}_i - \vec{r}_j\right|$ is the distance between atoms, and f_{ij} are the Jastrow factors, which, in this case, were limited to three forms corresponding to He-He, He-Cl and Cl-Cl interactions. A detailed account of the construction of the three Jastrow factors can be found elsewhere [3,6]. There are several interesting qualities that their final form maintains. When any two atoms come close together, it is assumed that their pairwise potential dominates the many-body Schrödinger equation. Therefore, as the distance between atoms i and j decreases, f_{ij} and subsequently ψ_T go to zero. Conversly, as an atom strays far from the center of mass of the cluster and the relative potential decays, the wave function also decays. In the Jastrow form, ψ_T is forced to decay as:

$$\psi_T(R) \approx \frac{e^{-\gamma\left|\vec{r}_i - \vec{r}_{cm}\right|}}{\left|\vec{r}_i - \vec{r}_{cm}\right|} , \qquad (3)$$

where

$$\gamma = \sqrt{\frac{2\, m\, E_b}{\hbar^2}} . \qquad (4)$$

Here, E_b is the binding energy of the atom and m is the reduced mass of the atom, both with respect to the remainder of the cluster. Using the He_nCl_2 cluster as an example, when a single He atom is found at a relatively large distance x from the center of mass, its corresponding Jastrow factor needs to dominate the wave function, or:

$$f^2_{He-Cl}(x)\, f^{n-1}_{He-He}(x) \approx \frac{e^{-\gamma x}}{x} . \qquad (5)$$

We assume that the bulk of the binding energy was due to the He-Cl interaction[3], so the limit as x becomes large of $f_{He\text{-}He}(x)$ was set to 1, this leaving:

$$f_{He-Cl}(x) \approx \sqrt{\frac{e^{-\gamma x}}{x}} . \qquad (6)$$

To obtain the best approximation for the expectation value for the Hamiltonian, the parameters of the Jastrow factors were varied in search of a minimum energy. Morse potentials were found to produce the best results for the Cl-Cl and He-Cl interactions. Experimental results [2] guided us to use the Hartree-Fock dispersion potential for the He-He interactions.

The actual Rayleigh-Ritz integral was evaluated using the Metropolis, Rosenbluth, Rosenbluth, Teller and Teller (M(RT)2) algorithm. [6] The M(RT)2 method samples probability distributions, so the integral of Equation 1 has to be manipulated into the form:

$$\langle H \rangle = \int \frac{H\, \psi_T(R)}{\psi_T(R)} \frac{\psi_T{}^2(R)}{\int \psi_T{}^2(R)\, dR}\, dR \qquad (7)$$

to be evaluated. In this case, the quantity:

$$P(R) \equiv \frac{\psi_T{}^2(R)}{\int \psi_T{}^2(R)\, dR} \qquad (8)$$

maintains the properties of a normalized probability density. Using an acceptance/rejection scheme, the integral itself is evaluated by summing

$$\frac{H\, \psi_T(R_{new})}{\psi_T(R_{new})} \qquad (9)$$

and dividing by the number of iterations M. R_{new} is obtained for each iteration by either using the value of R_{old} or accepting a new configuration obtained by randomly sampling small changes in each coordinate of R_{old}.

Sampled positions are accepted with a probability which is defined as:

$$A_{old \rightarrow new} = \min\left[1, \frac{P(R_{new})}{P(R_{old})}\right] . \quad (10)$$

This definition dictates that if the new configuration has a higher probability, $|\psi_T(R_{new})|^2$,than the old, then $A_{old \rightarrow new} = 1$. All configurations are saved, not only to be analyzed directly, but to be used in the GFMC calculations.

Green's Function Monte Carlo Method

With the GFMC, the ground state energy is computed exactly. While this is useful in itself, the result provides a qualitative measure of the accuracy of the variational trial wave function. The closer the ground state energy computed by the variational method is brought to that of the GFMC, the closer the model may be assumed to represent the actual wave function and subsequent configuration distributions. Failure to bring these values to within acceptable levels would raise questions about the accuracy of the unmodified Jastrow wave function.

The algorithm involves solving the Schrödinger equation:

$$(H + E_T)\psi(R,t) = (E_o + E_T)\psi(R,t) \quad (11)$$

with $\psi(R,t=0)$ assumed to be known and the constant E_T chosen to keep $(E_o + E_T) > 0$. This is done by casting the equation into integral form and iterating the results:

$$\psi(R,t+\Delta t) = \int \psi(R',t)\, G(R,R',\Delta t)\, dR' \quad (12)$$

where $G(R,R',\Delta t)$ is the short-time approximation Green's function. [4,5] In this case, $\psi(R,t=0)$ only needs to be a function of R. This is where the variational data become useful.

Since the configuration distribution produced with the $M(RT)^2$ method represents a set of discrete positions for the N atoms in the cluster, with sufficiently large M, this distribution can be viewed as a set of discrete configurations which approximate the probability density itself. From this, $\psi(R,t=0)$ can be tabulated in the form:

$$\psi(R,t=0) \approx \int \delta(R - R')\, \psi(R',t=0)\, dR' \quad (13)$$

This equation is simply an expression of the idea that $\psi(R,t=0)$ is represented by a large number of δ functions with coefficients $\psi(R',t=0)$.

The short-time approximation Green's function is developed under the context of what has been termed diffusion Monte Carlo, which appears surprising at the onset. The idea is that the time dependent Schrödinger's equation can be interpreted as a diffusion equation in imaginary time. Fortunately both the Green's functions and entire algorithms for solving diffusion equations numerically have been known for many years and are directly applicable.

The formal solution to the time dependent Schrödinger equation is:

$$\psi(R,t) = \sum_j \phi_j(R) \exp\left(-\frac{iE_j t}{\hbar}\right) \quad (14)$$

where ϕ_j and E_j are the eigenstates and eigenvalues for the time independent Schrödinger equation as well. The key is that in imaginary time, this solution is a sum of exponentially decaying terms. A diffusion process in imaginary time would result in the exponential decay of successive eigenstates with the ground state the last to degenerate. Since the constant, E_T, can be adjusted without altering ϕ_j , the ground state eigenvalue of the equation can be shifted to zero to keep the ground state wave function from dying off entirely. The ensuing iteration of Equation 12 results in a wavefunction which represents the ground state wave function as t becomes sufficiently large.

The final form of the Green's function is:

$$G(R,R',\Delta t) \cong \left[\frac{1}{\left(\sqrt{4\pi D\, \Delta t}\right)^{3N}} \exp\left(-\frac{(R-R')^2}{4\, D\, \Delta t}\right)\right]$$

$$\exp\left(-\frac{1}{2}\left\{v(R) + v(R') - E_T\right\}\Delta t\right) \quad , D = \frac{\hbar^2}{2m}, \quad (15)$$

and can be interpreted as the probability density describing the movement of a point source. If Δt is kept sufficiently small, the probability of a δ function propagating from R' to R in Δt can be sampled from the Gaussian part of the Green's function. The exponential part can be viewed as a weighting term. However, if Δt is large, the change in potential between R and R' will sufficiently distort the Gaussian characteristics of the probability distribution.

At this point, a simple algorithm could be used to iterate Equation 12. An ensemble of δ functions could be propagated individually with the Green's function. Each iteration of Equation 12 would result in a new ensemble. If E_T were picked to be approximately equal to E_o, the ensemble would fluctuate about an equilibrium number as t became sufficiently large. If E_T were greater than E_o, the weighting term would cause the ensemble to explode. If the value of E_T were below E_o, the numbers would fall to zero. The objective would be to locate the E_T value which resulted in a convergence. The variational ground state value would be the logical initial choice.

The GFMC implemented in this research, however, used a technique referred to as importance sampling. [5] In this technique, the variational trial wave function is used to

n	E_o(cm-1)	n	E_o(cm-1)
2	-3032.642±0.008	15	-3112.3+0.1
3	-3040.096±0.009	16	-3115.9±0.1
4	-3047.57±0.04	17	-3119.5±0.1
5	-3054.95±0.05	18	-3122.2±0.1
6	-3061.98±0.06	19	-3125.1±0.1
7	-3068.86±0.06	20	-3127.1±0.2
8	-3075.47±0.07	21	-3129.0±0.1
9	-3081.86±0.06	22	-3130.5±0.2
10	-3087.91±0.09	23	-3131.9±0.2
11	-3093.23±0.08	24	-3132.6±0.2
12	-3098.6±0.1	25	-3133.1±0.2
13	-3103.5±0.1	26	--3134.5±0.3
14	-3108.1±0.1	27	-3134.0±0.4
		28	-3134.0±0.3

Table 1
Ground state energies of He_nCl_2 calculated using the variational Monte Carlo method.

essentially guide the propagation to reduce both the convergence time and the variance of the result. E_o was evaluated using the identity:

$$E_o \equiv \frac{\int \psi_T(R)\, H\, \psi(R)\, dR}{\int \psi_T(R)\, \psi(R)\, dR} \,. \qquad (16)$$

This integral was numerically computed in a fashion similar to the variational method. Since the Hamiltonian is a Hermetian operator, $\psi_T(R)$ and $\psi(R)$ can be commuted with H and the integral takes the form:

$$E_o = \int \left[\frac{H\,\psi_T(R)}{\psi_T(R)}\right] \frac{\psi_T(R)\,\psi(R)}{\int \psi_T(R)\,\psi(R)\,dR}\, dR \,. \qquad (17)$$

As in the M(RT)2 procedure, the right term was treated as a probability distribution and the left was averaged over the number of samplings M.

RESULTS

Values of the variational Monte Carlo ground state energies for n between 2 and 28 are shown in Table 1. Due to the considerable cpu time required for convergence of the GFMC algorithm, values for the ground state energies computed by the GFMC are provided for n = 8, 18 and 28 in Table 2. Per particle differences in the variational and GFMC values are consistent at roughly 1.5cm-1. That the variational values converged at n greater than 25 probability suggests that for this number of particles, the Jastrow factors should be altered. It is likely that the He-He interactions are providing a significant amount of binding energy to the cluster. In this situation, $f_{\text{He-He}}(r)$ would have to decay as well.

n	E_o(cm-1)
8	-3086.7±0.1
18	-3149.5±0.3
28	-3171±7†

Table 2
Ground state energies of He_nCl_2 calculated using the Green's function Monte Carlo method.
† More computer time would have resulted in a stronger convergence and subsequent lower error.

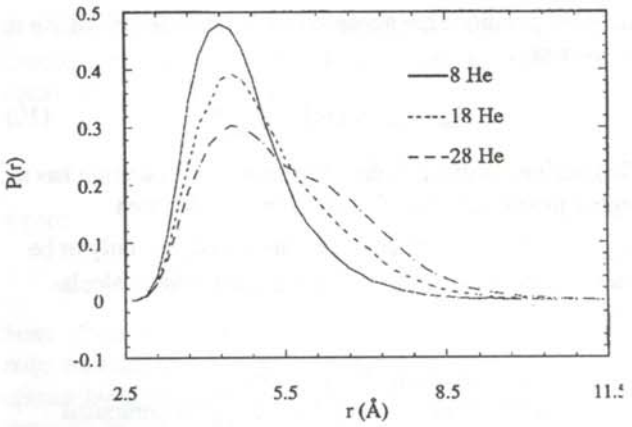

Figure 2
Histogram of the probability distributions in r for clusters with 8, 18 and 28 helium atoms.

Probability distributions for the ground state variational calculations posses a striking consistency for clusters containing 2 to 28 helium atoms. Figure 2 shows histograms of radial distributions for the cases of n=8,18 and 28. The distributions for all values of n have a broad base

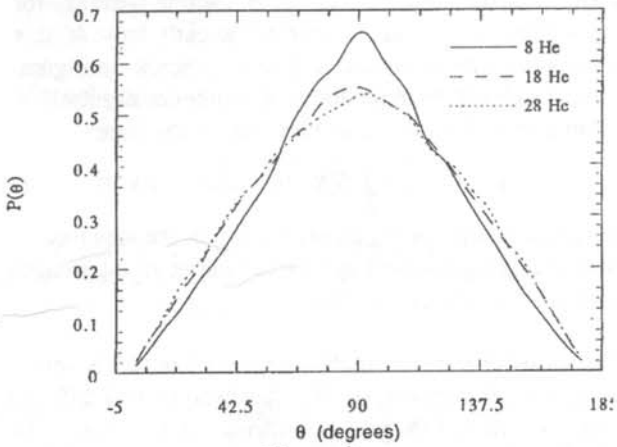

Figure 3
Histograms of probability distributions in θ for clusters with 8, 18 and 28 helium atoms.

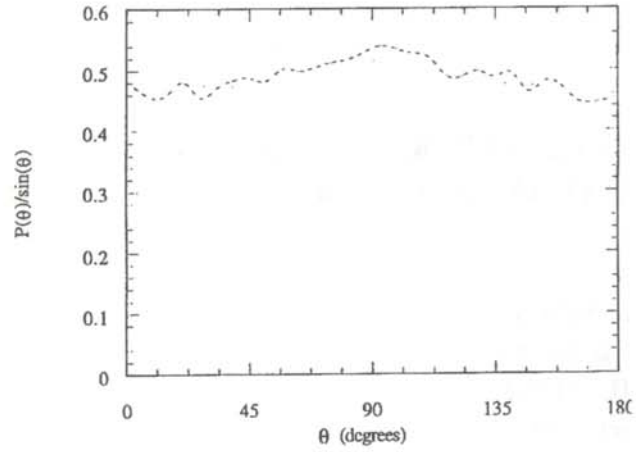

Figure 4

Histogram of the probability distribution of θ divided by sin(θ). Since the number of helium atoms which can be placed at angle θ is proportional to sin(θ), this generally horizontal graph suggests a uniform distrbuition of angles between 0° and 180°.

with a maximum between 4Å and 4.5Å. Throughout this range of n, minimum values of r are fixed near 2.5Å. The maximum value for r gradually increases with the number of helium atoms. Probabilities diminish at about 5.5Å for n=2 and fade at roughly 10Å for n = 28. The right-hand shoulder develops slowly with an apparent emergence at n = 17 or n = 18.

Histograms of angular distributions are similar as well. Figure 3 shows the profiles in θ for the cases where n = 8, 18 and 28. With n values between 15 and 28, symmetry in the histograms suggest uniformity in the angular distributions of the helium atoms about the chlorine molecule.

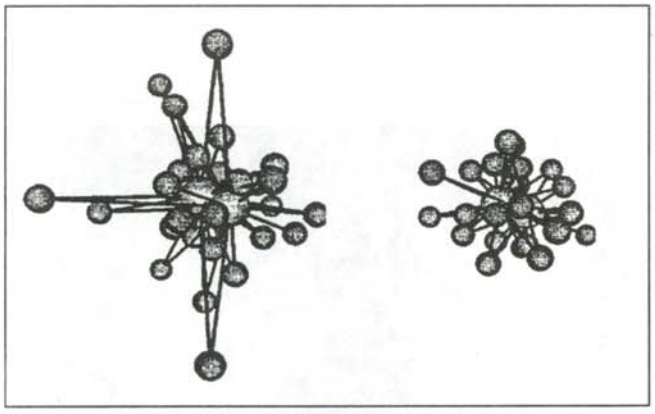

Figure 5

Models of the ground state of the $He_{28}Cl_2$ cluster showing configurations with helium atoms place at a relatively large distance from the Cl_2 center of mass, and a model showing a relatively compact cluster.

Figure 4 is a plot of $P(\theta)$ divided by $\sin(\theta)$ for $He_{28}Cl_2$. It shows a general uniformity of the probability for angles from 0° to 180°. This suggests that the distributions are generally spherical. Examples of the resulting ground state clusters are shown in Figure 5. It appears to take the form of a liquid which engulfs the chlorine molecule. The variation in the two ground state clusters shows that there is a considerable fluctuation in the r coordinate producing a broad range of fluctuations in atomic configuration.

ACKNOWLEDGMENTS

Special thanks is extended to Dr. Kevin E. Schmidt for his gracious mentorship. Computation support was provided by the Ohio Supercomputer Center. This work was performed under the auspices of the Arizona State University Physics Research Experience for Undergraduates Program, supported by the National Science Foundation and Arizona State University.

REFERENCES

* Present Address of the author: Department of Mathematics and Computer Science, Colorado School of Mines, Golden, CO 80401.

1. W.D. Sands, C.R. Bieler and K.C. Janda, J. Chem. Phys, 95, (1991), p. 729.
2. R.A. Aziz, V.P.S. Nain, J.S. Carley, W.L. Taylor, G.T. McConville, J. Chem. Phys, 90, (1979), p. 4330.
3. Z. Bacic, M. Kennedy-Mandzuik, J.W. Moskowitz and K.E. Schmidt, J. Chem. Phys., 97, (1992), p. 6472.
4. M.A. Lee and K.E. Schmidt, Comput. Phys., 6, (1992), p. 192.
5. P.J. Reynolds, J. Tobochnik and H. Gould, Comput. Phys., 4, (1992), p. 662.
6. K.E. Schmidt, Models and Methods in Few-Body Physics, (1987), p. 273.

FACULTY SPONSOR

Dr. Kevin Schmidt
Department of Physics and Astronomy
Arizona State University
Tempe, AZ 85287-1504
schmidt@phyast.la.asu.edu

A LATTICE GAS APPROACH TO THE STRUCTURE AND DYNAMICS OF ELECTRORHEOLOGICAL FLUIDS

Jie Chen *
Department of Physics
Illinois Wesleyan University
Bloomington, IL 61702
received September 7, 1993

ABSTRACT

Electrorheological fluids consist of a colloidal suspension of dielectric particles in a continuous fluid of smaller dielectric constant. Recent molecular dynamics simulations of these fluids in an applied electric field have been shown to produce percolated, columnar structures.[1] No systematic attempt has been made so far to simultaneously include the effects of temperature and viscous drag due to the continuous fluid. We propose a dipolar lattice gas model to study the resulting structures and dynamics. We incorporate the effect of viscosity of the continuous medium by a dynamic ansatz that determines the range over which individual particles can jump in a single simulation event. The temperature is simulated by assigning a probability of jumping to higher energy states in accordance with the Boltzman distribution. We study the equilibrium phases of the system as a function of temperature. Our results from finite temperature simulations suggest that there is a gradual phase transformation from a liquid like phase at low electric field or equivalently at high temperature to a solid like phase at high electric or at low temperature.

1. Jaggi, N.K. Jour. Stat. Phys., 64, (1991), p. 1093.

INTRODUCTION

Electrorheological (ER) fluids are a class of novel materials that have received considerable attention recently. [1-6]. They consist of small, highly polarizable, solid particles, suspended in low dielectric constant fluids. One interesting characteristic of these fluids is that when an electric field is applied across them, the viscosity increases almost immediately by a very large amount. They behave more like a weak solid than a liquid. When the electric field is removed, they revert almost instantly back to the liquid state. Because of the ease and small expense of generating electric fields and the short response time to the applied fields (on the order of a millisecond), these fluids have many potential applications, such as the next generation of low cost active automotive suspensions, brake and transmission systems.

Since the particles suspended in the continuous medium are relatively large (1-5μm), the structure of the ER fluid can be studied directly by optical microscopy. Figure 1 shows a recent result [1] for such a photograph. The particles seem to cluster and form chain like structures

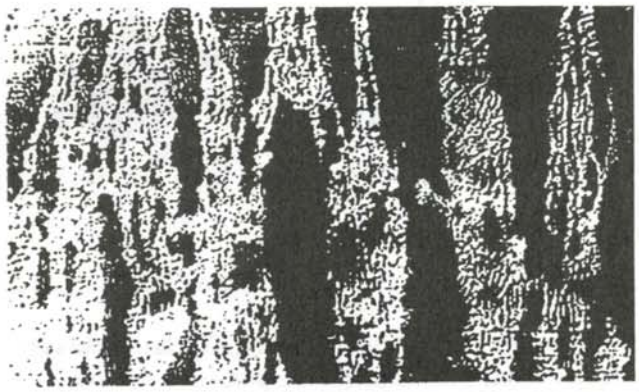

Figure 1
Micrograph of the structure of an ER fluid from Whittle[1].

The author graduated from Illinois Wesleyan University in 1993 with a Bachelors in physics. He is now pursuing a Ph.D. degree at the University of Chicago and is working in the Frank Center for Image Analysis. His current research interests are in the area of medical physics and in image processing. He is a recipient of a Grant-in-Aid for research from Sigma-Xi. He is a member of the Society of Physics Students and an associate member of Sigma-Xi.

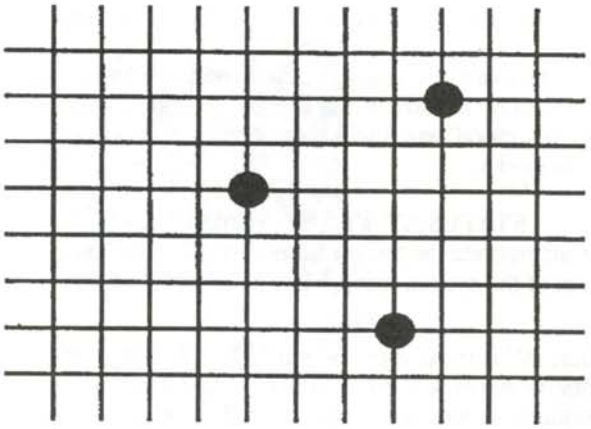

Figure 2
Schematic diagram of the lattice grid showing three occupied sites used in our model.

along the direction of the electric field. These chain -like structures are not simple straight lines, but are intertwined and twisted. The width of the columns changes significantly as one moves along the field direction. As a result of this columnar structure, the viscosity of the fluids increases as the chains become longer and thicker.

During the past 5 years, a consensus seems to have emerged that there are basically three types of phenomena that dominate the physics during the transformation [2]: The induced dipole interactions among these small particles; the viscous drag forces on the particles as they move through the continuous medium; and the thermal fluctuation of the system at finite temperatures. The forces involved are quite complex, they are long range and anisotropic. It is a many-body problem. It has not been possible to solve the problem analytically. Most of the progress in understanding these complex fluids has been made by computer simulations [3,4,5]. The results are in agreement with the structures obtained experimentally, but there are still some interesting questions which have not been explored.

DIPOLAR LATTICE GAS APPROACH

Previous computer simulations use continuous models in which the particles can move freely in the continuum according to Newtonian mechanics. In our model, we restrict the positions of the particles on a lattice grid. The particles can only occupy the intersections of the lattice. No two particles can occupy the same position. We use an energy based adaptive Monte Carlo algorithm to simulate the dynamics. This is described in greater detail in the following sections. In this paper, we focus on the two dimensional square lattice.

There are fluctuations in local density, but the overall density of the system is held constant through out the transformation. Since there is a repulsive component in the dipole interaction, we introduce the following boundary conditions to keep the overall density constant. When ever a particles moves out of the left boundary, it is introduced back to the corresponding position on the right side, as if the lattice grid were circular in the horizontal direction. The same prescription is applied to particles moving out of the right boundary. Since the top and bottom boundaries represent the two metallic electrodes, the particles are not allowed to jump out of the top and bottom boundaries. Mirror image boundary conditions are applied as required by the theories of electromagnetism.

STRUCTURE AND DYNAMICS AT ZERO TEMPERATURE

The system begins with a certain density of randomly placed particles on the lattice. As the electric field is applied across the lattice, the particles become induced dipoles in the direction of the external electric field. The electrostatic force F_i on the i^{th} dipole is:

$$F_i = -\nabla_i U(r_j)$$
$$= 3p^2 \sum_j \frac{1}{r_{ij}^4}\left[\{3\cos^2(\theta_{ij}) - 1\}\hat{e}_r + \{\sin(2\theta_{ij})\hat{e}_\theta\}\right] \quad (1)$$

where p is the induced dipole moment in the direction of the applied electric field, r_{ij} is the distance between particles i and j, θ_{ij} is the angle between the vector $\mathbf{r}_{ij}$ and the direction of the electric field. The energy of the system $U(r_j)$ is given by:

$$U(r_j) = -p^2 \sum_{i,j} \frac{\{3\cos^2(\theta_{ij}) - 1\}}{r_{ij}^3} \quad (2)$$

with the sum running over all dipoles and their sequence of images in the two metallic electrodes. At zero temperature, because of the viscous drag force, the system will

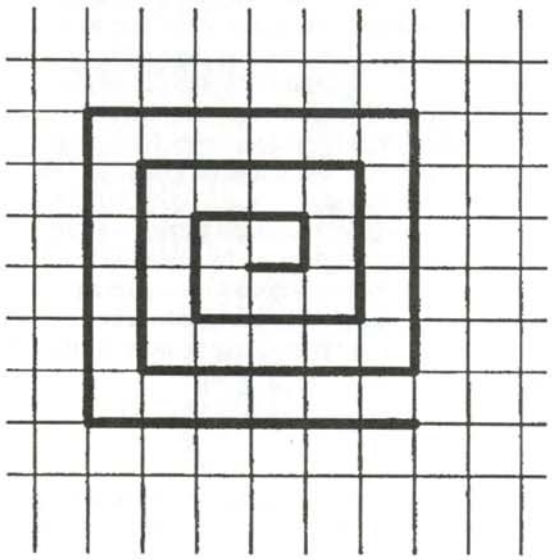

Figure 3
Schematic diagram of the Outward Spiral Search Algorithm.

evolve in the direction of decreasing energy.

Each particle has a "neighborhood", the square area, with the particle at its center within which the particle can attempt to jump in a single move. A random target empty lattice site is selected within the "neighborhood" . If this tentative move can lower the total energy, we accept it and repeat the procedure on another randomly selected particle. If this does not lower the total energy, we go on and try another empty site in the "neighborhood" until all the empty sites within the "neighborhood" have been exhausted. This whole procedure it iterated again for another "neighborhood" until we stop it.

Our first attempt at choosing an empty site within the "neighborhood" was to check all possible sites within the specified "neighborhood" and find the one that can lower the total energy the most and then move the particle to that site. This method does give us the steepest decrease in energy, but it needs to check every possible site in the "neighborhood" . It is computationally too expensive as we go to larger lattices.

Another way of deciding where to jump is to move as soon as we find a site than can lower the energy. We want to make sure that the final stricture of the system is the result of the underlying physics, not due to the algorithm we use to find the target site. If we search for the target site in the "neighborhood" starting from the north-west corner moving sequentially down to the south-east corner, there is a tendency for particles to cluster in the north-west corner. To eliminate this, we adopted a dynamic ansatz which we call *Outward Spiral Search Algorithm* which is shown in Figure 3. We shall first check the near "neighborhood" of the particle. If the sites in the near "neighborhood" cannot lower the energy, then we search for outer neighborhood sites. Since the dipole interaction decreases as $1/r^3$, the farther away the particles, the less their influence. We introduced a "range" parameter as the cut off during the summation. It is also specified as a square area. If a particle sits outside the "range-square", centered at the current particle, their mutual interaction is ignored.

The formal criterion for moving a particle to a new site is related to the total energy given by Equation 2. In practice, however, we only need to compute a partial energy U_i, which is a single sum of interaction energies of the particle that we are attempting to move with the other particles in the system.

$$U_i = -p^2 \sum_{i \neq j} \frac{\{3\cos^2(\theta_{ij}) - 1\}}{r_{ij}^3} \qquad (3)$$

Since we move one particle at a time, the relative positions of the other particles are unchanged. The energy associated with those particles does not change either. To determine whether the new move can lower the total energy, we only need to know if the move can lower the partial energy associated with the particle itself. This method results in significant computational savings.

We hope that the viscosity of the continuous medium is simulated by the size of the "neighborhood" . Larger "neighborhood" sizes will correspond to less viscous liquid media.

STATES AT FINITE TEMPERATURE

We incorporate the temperature effects on the equilibrium states of the system using a Boltzman distribution:

$$P(\Delta U) = e^{-\frac{\Delta U}{kT}} . \qquad (4)$$

where ΔU is the energy difference before and after the tentative move, k is the Boltzman constant and T is the absolute temperature. For a fixed positive ΔU, the higher the temperature, the larger the probability that it can jump to the higher energy states. We guarantee this distribution in the simulation with the following procedure. At each tentative move, ΔU is calculated. If $\Delta U<0$, the tentative move is accepted. If $\Delta U > 0$, the probability $P(\Delta U)$ is calculated. A random number is drawn. If the number is smaller than the calculated probability, the tentative move is accepted. Otherwise, the tentative move is rejected. After many trials, the frequency of accepting moves to higher energy states is in accordance with the Boltzman distribution.

RESULTS

Zero Temperature

At zero temperature, the total energy of the system decreases monotonically with time as shown in Figure 4, for a 100 x 100 lattice. The structure of the system at times 0, 2 and 11 are shown in Figure 5. The system begins with a random configuration. After the electric field is applied across it, the particles cluster to form short chains. At time 2, the chain-like structures are becoming longer in the direction of the electric field. As the system evolves, the columnar structure becomes longer and thicker. At time 11, the columnar structures completely span the two electrodes and are all intertwined together. Our approach generates results that are in reasonable agreement with previous experimental and computational

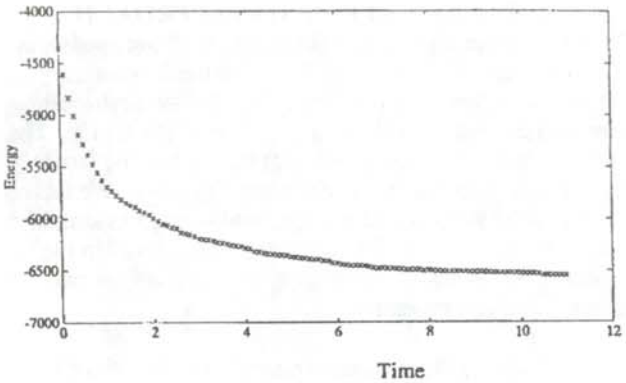

Figure 4
Total energy vs. time for a 100x100 lattice at T = 0

Figure 5
Three structures at times t = 0.2.11, showing the formation of the intertwined columns.

works. This gives us the confidence to go beyond the structure and dynamics at $T = 0$ and study the thermodynamic properties of the ER fluids at finite temperatures, which has not been explored earlier.

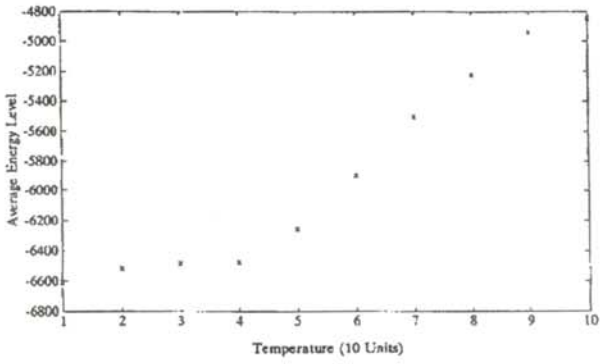

Figure 6
Average energy of the system vs temperature.

Temperature Effects on the Equilibrium States
At finite temperature, the particles have a certain probability to jump to a higher energy state. Since the system is continuously changing, there is no single final structure for it. After a sufficiently long time, the system will reach its thermodynamic equilibrium state. At equilibrium, the structure and energy will fluctuate around an average structure and energy. At a fixed temperature, the average total energy of the system is constant over a long period of time. Figure 6 is a plot of the average total energy vs. temperature. There is a gradual transition from low average energy at low temperature to high average energy at high temperature. Figure 7 shows some typical structures for the system at these different temperatures (T= 2, 4, 6, 8, 10). At low temperature, the equilibrium state of the system is well ordered, which is like a solid. At high temperature, the columnar structures are broken up, producing a disordered system, one more like a liquid. There is a gradual transition from well ordered to disordered as the temperature increases, which correlates with the gradual transition of the average energy. We see no sharp transition such as occurs in a true phase transition. This is in agreement with almost all of the experimental results[3,6].

Since the temperature effects are simulated by assigning probabilities of jumping to higher energy states according

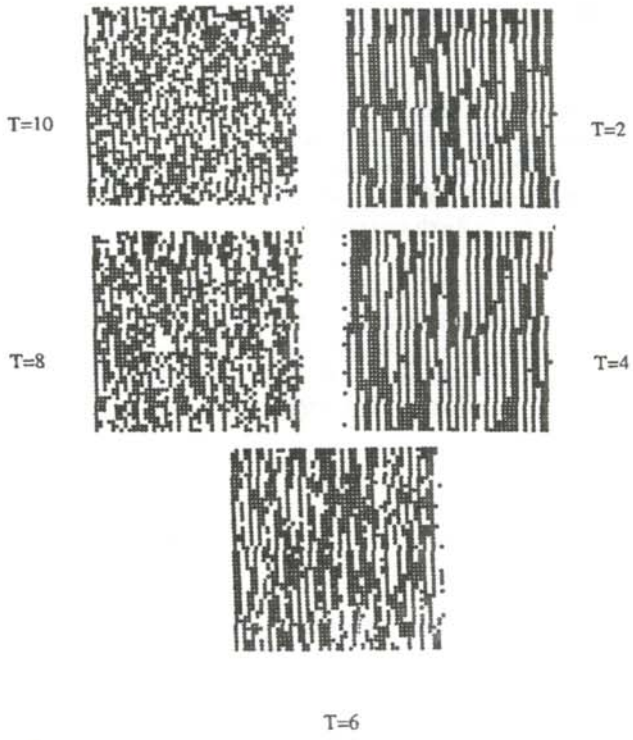

Figure 7
Typical structures of the equilibrium states at different temperatures showing how the system disorders at higher temperatures.

to the Boltzman distribution, the structure is determined by the ratio of energy difference to temperature. This means that high electric field strength is equivalent to low temperature and vice versa.

ACKNOWLEDGMENTS

The author would like to express his sincere thanks to Dr. Narendra Jaggi for his collaboration on this research project and for his encouragement and guidance. He would also like to thank Garrett Davis for various discussions and helpful suggestions. This work was supported by a NASA/JOVE grant #NAG-8-268 to Illinois Wesleyan University Physics Department.

REFERENCES

* Current address of the author: Frank Center for Image Analysis, University of Chicago, Chicago, IL 60615.

1. Whittle, M. Physics World,2, (1989), p. 39.
2. Gast, A.P. and C.F. Zukoski, Advances in Colloid and Interface Science, 80, (1989), p. 153.
3. Klingenberg, D.J. F. van Swol and C.F. Zukoski, Journal of Chemical Physics, 91, (1989), 0. 7888.
4. Bonnecaze, R.T. and J.F. Brady, Electrorheological Fluids: Proceedings of the Second International Conference on ER Fluids, (1990), p.27.
5. Jaggi, N.K., Journal of Statistical Physics, 64, (1991), p. 1093.
6. Payne, J.A. and N.K. Jaggi, Bulletin of the American Physical Society, 38, 1993, p. 236.

FACULTY SPONSOR

Dr. Narendra K. Jaggi
Laboratory for Materials Physics
Illinois Wesleyan University
Bloomington, IL 61702-3902
jaggi@uxh.cso.uiuc.edu

PERTURBATIVE SOLUTION FOR NONLINEAR WAVES ON A STRETCHED STRING

Will Holmes
Department of Physics
Southern Nazarene University
Bethany OK 73008
received October 10, 1993

ABSTRACT

We present a derivation of a nonlinear differential equation for the motion of a stretched string that is fixed at both ends. The nonlinear terms are parameterized in terms of a "degree of smallness", λ. A perturbation expansion to order λ^2 and a Green's function allow us to solve this equation to second order. We show a plot of the solution in space and time.

INTRODUCTION

For a stretched string with linear density μ and tension *T*, as shown in Figure 1, Newton's second law for the direction transverse to the string becomes:[1,2]

$$T\left(\sin\left(\theta_2\right) - \sin\left(\theta_1\right)\right) = \left(\mu\,\Delta x\right)\frac{\partial^2 y}{\partial t^2}\ , \qquad (1)$$

where Δx is a segment of length. If one assumes that the angle is sufficiently small so that:

$$\sin\left(\theta\right) \cong \tan\left(\theta\right) = \frac{\partial y}{\partial x} \qquad (2)$$

and takes the limit as Δx approaches 0, the well-known linear wave equation:

$$\frac{\partial^2 y}{\partial x^2} = \left[\frac{1}{V^2}\right]\frac{\partial^2 y}{\partial t^2} \qquad (3)$$

appears, where the wave speed V is given by:

$$V = \sqrt{\frac{T}{\mu}}\ . \qquad (4)$$

Will will graduate from Southern Nazarene in May with a B.Sc. in physics and mathematics. This research was done in his junior year. Will enjoys all aspects of campus life, especially ultimate frisbee, basketball and dorm life. He plans to go to graduate school, but is still undecided where to go.

If, however, we have a case where Equation 2 is not a good approximation, Equation 1 becomes:[3]

$$\frac{y''}{\left(1+y'^2\right)^{\frac{3}{2}}} = \left[\frac{1}{V^2}\right]\ddot{y}\ , \qquad (5)$$

where:

$$y'' = \frac{\partial^2 y}{\partial x^2} \qquad \ddot{y} = \frac{\partial^2 y}{\partial t^2}\ . \qquad (6)$$

In going from Equation 1 to Equation 5, we have used:

$$\tan\left(\theta\right) = \frac{\partial y}{\partial x}\ . \qquad (7)$$

PERTURBATIVE SOLUTION

We now solve the differential equation (Equation 5). If the term responsible for the non-linearity, y'^2, is not small enough to neglect, but is small enough that a perturbative solution will converge rapidly, a perturbative expansion is

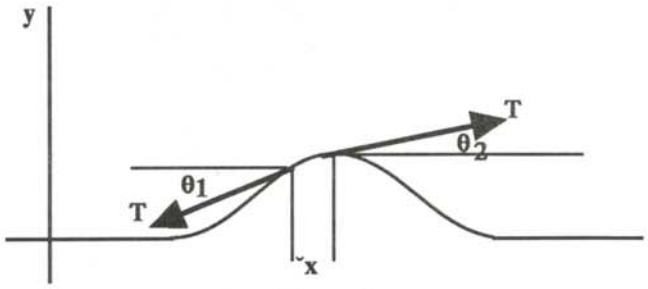

Figure 1
Sketch of a section of a string under tension showing the tension and the angles.

a useful model for this system. We assume that the string meets these criteria, and that the solution is a series of the form:

$$y = \lambda^0 y_0 + \lambda^1 y_1 + \lambda^2 y_2 + \ldots \quad . \tag{8}$$

The dimensionless parameter λ is introduced to keep track of the "degree of smallness". Note that the nth order solution has λ^n attached to it. When Equation 8 is used to solve Equation 5, all the terms with the nth power of λ will correspond to y_n. We keep track of the "degree of smallness"[4] of the nonlinear term in Equation 5 with the same parameter λ by writing:

$$\frac{y''}{\left(1+\lambda y'^2\right)^{\frac{3}{2}}} = \left[\frac{1}{V^2}\right] \ddot{y} \tag{9}$$

We now solve equation 9 by performing a binomial expansion of the radical and substituting the derivatives of Equation 8 into Equation 9, which becomes:

$$\begin{aligned}&[y_0'' + \lambda y_1'' + \lambda^2 y_2''][1 - \tfrac{3}{2}\lambda y_0'(y_0' + \lambda y_1' + \lambda^2 y_2') \\ &- \tfrac{3}{2}\lambda^2 y_1'(y_0' + \lambda y_1' + \lambda^2 y_2') - \tfrac{3}{2}\lambda^3 y_2'(y_0' + \lambda y_1' + \lambda^2 y_2') \\ &+ \tfrac{15}{8}\lambda^2(y_0'^2 + \ldots)] \cong \frac{1}{V^2}\left(\ddot{y}_0 + \lambda \ddot{y}_1 + \lambda^2 \ddot{y}_2\right)\end{aligned} \tag{10}$$

Collecting terms with like powers of λ, we have to $O(\lambda^0)$:

$$y_0'' - \frac{1}{V_o^2}\ddot{y}_0 = 0 \ , \tag{11}$$

to $O(\lambda^1)$:

$$y_1'' - \frac{1}{V_1^2}\ddot{y}_1 = \frac{3}{2} y_0'^2 y_0'' \ , \tag{12}$$

to $O(\lambda^2)$:

$$y_2'' - \frac{1}{V_2^2}\ddot{y}_2 = -\frac{15}{8} y_0'^4 y_0'' + 3 y_0'' y_0' y_1' + \frac{3}{2} y_1'' y_0'^2 \ . \tag{13}$$

Equation 11 is just the linear case, so to 0th order, we recover the linear approximation. Equations 11-13 all have the form:

$$\Box^2 y_n = F_n \ , \tag{14}$$

where F_n is a function of y_m for m<n, and

$$\Box^2 = \frac{\partial^2}{\partial x^2} - \frac{1}{V^2}\frac{\partial^2}{\partial t^2} \tag{15}$$

is the d'Alembertian operator.

Equation 8 indicates that the total solution to the nonlinear wave equation is the linear solution plus some correction terms. These correction terms can be found since their solution depends only upon lower order terms. We use the well known solution for the linear case, chosen to satisfy the boundary conditions that the end points at $x = 0$ and $x = L$ are nodes:

$$y_0 = A \sin\left(k_o x\right) e^{-i\omega_o t} \ , \tag{16}$$

where $k_o = n\pi/L$ and $V_o = \omega_o/k_o$. The most general unperturbed linear solution is a Fourier series of such solutions, but we shall assume a monochromatic unperturbed solution.

We now turn our focus to solving for the first correction term y_1. Assuming that y_1 can be factored into space dependent and time dependent functions in the same way as was done in Equation 16,

$$y_1(x,t) = h_1(x)\, e^{-i\omega_1 t} \ , \tag{17}$$

Equation 11 becomes:

$$\begin{aligned}&e^{-i\omega_1 t}[h_1'' + k_1^2 h_1] = \\ &\quad - e^{-i3\omega_0 t}\frac{3}{2}[A^3 k_0^4 \cos^2\left(k_0 x\right)\sin\left(k_0 x\right)],\end{aligned} \tag{18}$$

where

$$k_1 = \frac{\omega_1}{V_1} \ . \tag{19}$$

Equation 18 can be simplified to:

$$\begin{aligned}&e^{-i\omega_1 t}[h_1'' + k_1^2 h_1] = \\ &- e^{-i3\omega_0 t}\frac{3}{8}[A^3 k_0^4 \{\sin\left(k_0 x\right) + \sin\left(3k_0 x\right)\}]\end{aligned} \tag{20}$$

For Equation 20 to be true for all time:

$$\omega_1 = 3\omega_0 \tag{21}$$

Since the right hand side of equation 18 is not zero, $k_1 \neq 3k_o$. The relationship between k_1 and k_o will be determined later. Substituting Equation 21 into Equation 20 allows the time dependence to be factored out, resulting in an equation for $h_1(x)$:

$$[h_1'' + k_1^2 h_1] = \frac{3}{8}[A^3 k_0^4 \{\sin\left(k_0 x\right) + \sin\left(3k_0 x\right)\}] \ . \tag{22}$$

Finding $h_1(x)$ using a Green's Function

Equation 20 can be solved by variation of parameters or by a Green's function. The latter is a technique for solving inhomogeneous differential equations. If

$$D\psi(x) = F(x) \tag{23}$$

where D is a differential operator and if

$$D\, G(x - x') = \delta(x - x') \tag{24}$$

where $\delta(x - x')$ is the Dirac delta function and $G(x - x')$ is the Green's function, the solution to Equation 23 is:

$$\psi(x) = \int G(x - x')\, F(x')\, dx' \tag{25}$$

where the integration is over all space. If we know how the system responds to an impulsive or point source, the solution, $\psi(x)$ is a summation of responses to impulsive sources weighted by the density function $F(x')$.

Putting Equation 20 into the form of Equation 23:

$$\left[\frac{d^2}{dx^2} + k_1^2\right] h_1 = \frac{3}{8} A^3 k_0^4 \left\{\sin\left(k_0 x\right) + \sin\left(3k_0 x\right)\right\} , \tag{26}$$

For this differential operator and the boundary conditions that $x = 0$ and $x = L$ are nodes, the Green's function is:[5]

$$G(x - x') = \begin{cases} \dfrac{\sin(k_1 x')\sin(k_1[x - L])}{k_1 \sin(k_1 L)} & 0 < x' < x \\ \dfrac{\sin(k_1 x)\sin(k_1[x' - L])}{k_1 \sin(k_1 L)} & x < x' < L \end{cases} \tag{27}$$

Using Equation 25 to solve Equation 22, we have:

$$h_1 = -\frac{3A^3 k_0^4}{8 k_1 \sin(k_1 L)}\Big[\sin(k_1[x-L])\, I(x) + \sin(k_1 x)\, J(x)\Big] \quad (28)$$

where

$$I(x) = \int_0^x \sin(k_1 x')\left\{\sin(k_0 x') + \sin(3k_0 x')\right\} dx' \quad (29)$$

and

$$J(x) = \int_x^L \sin(k_1[x'-L])\left\{\sin(k_0 x') + \sin(3k_0 x')\right\} dx' \quad (30)$$

Evaluating the integrals with the help of some trigonometric identities gives $h_1(x)$ as:

$$h_1(x) = B\left\{\sin(k_1[x-L])\, M(x) + \sin(k_1 x)\, N(x)\right\}, \quad (31)$$

where

$$B = \frac{3A^3 k_0^4}{16 k_1 \sin(k_1 L)}, \quad (32)$$

and

$$M(x) = \frac{\sin[(k_1+k_0)x]}{k_1+k_0} - \frac{\sin[(k_1-k_0)x]}{k_1-k_0} + \frac{\sin[(k_1+3k_0)x]}{k_1+3k_0} - \frac{\sin[(k_1-3k_0)x]}{k_1-3k_0} \quad (33)$$

and

$$N(x) = \frac{\sin[k_1 L-(k_1+k_0)x]}{k_1+k_0} - \frac{\sin[k_1 L-(k_1-k_0)x]}{k_1-k_0} - \frac{\sin[k_1 L-(k_1-3k_0)x]}{k_1+3k_0} + \frac{\sin[k_1 L-(k_1+3k_0)x]}{k_1+3k_0} \quad (34)$$

INTERPRETATION OF RESULTS

We can specify a value for k_1 by applying the boundary conditions to Equation 22. Since both h_1 and the right hand side of Equation 22 equals 0 at both $x=0$ and $x = L$, h_1'' must also equal 0 at these points. Taking the second derivative of Equation 31 and setting it equal to 0 results in:

$$\cos(k_1 L) = 0 . \quad (35)$$

Therefore,

$$k_1 = \frac{(2m-1)\pi}{2L}, \quad (36)$$

where m is an integer greater than 1. In general, m will range from 1 to ∞, but in many cases, it is only necessary to consider values from 1 to 3 because contributions with larger m are very small. The greater the amplitude, the more terms one is obliged to include.

The ratio of the amplitudes for the first perturbed term and the linear term is:

$$\frac{y_1}{y_0} = \frac{h_1(x)}{A\sin(k_0 x)}. \quad (37)$$

Using Equation 31 for h_1, recalling that $k_0=n\pi/L$ and using Equation 36 gives the approximate ratio:

$$\frac{y_1}{y_0} \cong -\frac{3}{8}\frac{n^4\pi^3}{2m-1}\frac{A^2}{L^3} \quad (38)$$

where we neglect the terms inside the brackets in Equation 31 that contain k. This causes the ratio to appear to have dimensions of length^{-1}.

We now can find a value for $V_1 = \omega_1/k_1$, the speed of the first-order correction to the wave function. We determined ω_1 and k_1 completely independently from V_1. This implies that the velocity is dependent upon m. Hence, V_1 may "adjust" so that all k_1's will be present. This suggests dispersion, and the need for a Fourier series for the first-order perturbation. Fortunately, as can be seen from Equation 37, this series converges in a few terms.

To help the reader visualize these results, we plotted the first two terms of the total wave function:

$$y = y_0 + y_1 \quad (39)$$

or

$$y = \cos(\omega_0 t)\sin(k_0 x) + \cos(\omega_1 t)\, h_1(x) \quad (40)$$

with the value of $n = 1$ (see Equation 16) and making a superposition with values of m ranging from 1 to 3. Figure 2 shows these results.

We have used a familiar physics problem, waves on a stretched string, as an example of a nonlinear system. We constructed a solution to this problem using perturbation techniques. This example offers a useful tool, in a familiar system, for introducing the reader to the challenges that one must face in an analytical approach to nonlinear physics.

ACKNOWLEDGMENTS

The author would like to thank Dr. Neuenschwander for the idea, his encouragement and for many great discussions.

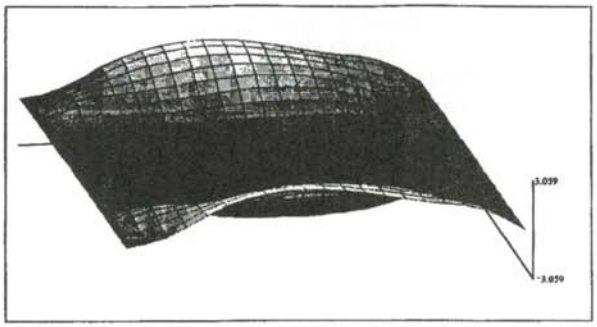

Figure 2

This is a plot of Equation 40. It shows how the wave develops in time as well as in space. The x axis is the horizontal axis and the time axis comes out of the page. The plot shows one complete cycle with an arbitrary length of 10 and an amplitude of 3.

REFERENCES

1. Paul Tipler, Physics, 2nd edition, Worth Publishers, New York, 1982, pp. 433-435.

2. Raymond Serway, Physics, 3rd edition, Saunders College Publishing, Philadelphia, 1990, pp. 447-448.

3. Dwight Neuenschwander, Structures and Interactions in Nature (A draft of a text for the Introductory University Physics Project, unpublished, 1993), pp. 484-487.

4. David Saxon, Quantum Mechanics, Holden-Day, San Francisco, 1968, p. 190.

5. John Mathews and R.L. Walker, Mathematical Methods of Physics, 2nd edition, W.A. Benjamin, Inc., Reading , 1970, p. 270.

FACULTY SPONSOR

Dr. Dwight Neuenschwander
Department of Physics
Southern Nazarene University
Bethany, OK 73008

A NOVEL TECHNIQUE FOR STUDYING THE SHEAR ELASTIC PROPERTIES OF WEAK SOLIDS

Jason A. Payne*
Department of Physics
Illinois Wesleyan University
Bloomington, IL 61702
received September 5, 1993

ABSTRACT

We have developed a simple, inexpensive and precise technique for measuring the shear elastic modulus of weak solids using electromagnetic and optical tools. This technique can be adapted to measure the viscosity of a liquid as well. A Helmholtz pair was used to produce a torque on a permanent magnet mounted on the smaller of two concentric cylinders, coupled by the material to be studied. The torque was controlled precisely and measured accurately in terms of the current flowing through the coils of the Helmholtz pair. An optical lever was employed to measure the angular displacement of the inner cylinder as a function of the applied shear stress. The instrument was validated by making measurements on lemon jello and agarose gels of varying concentrations. The instrument has also been used to study the electric field induced "freezing" of electrorheological fluids, a subject of contemporary interest.

INTRODUCTION

Traditionally, the shear elastic properties of solids have been measured using mechanical instrumentation. The material under study is typically grabbed and then twisted or stretched. The angular displacement, or change in length, is then measured by either mechanical or electronic methods. Results of the measurements are frequently presented as stress-strain (τ–γ) graphs, such as shown in Figure 1, where τ denotes the shear stress and γ represents the shear strain. A solid typically behaves linearly over a finite region of stress and eventually moves into a nonlinear region. This nonlinear behavior terminates when the material fails. The slope of the linear region of the (τ–γ) graph is the elastic modulus of the material understudy. In this study, we are interested in the static shear modulus, G, defined as:

$$G = \lim_{\gamma,\dot{\gamma}\to 0} \frac{\Delta\tau}{\Delta\gamma} \qquad (1)$$

where $\dot{\gamma}$ is the time rate of change of the strain, called the strain rate.

Gels, foams and electrorheological fluids are typical examples of a class of materials that have been grouped under the label "complex fluids". The importance of these materials in such areas as automotive engineering, robotics and chemical engineering warrant close investigation of their properties under different conditions. They are also

The author is currently a Ph.D. candidate in the Chemical Engineering and Materials Science Department at the University of Minnesota-Twin Cities. His current research involves the study of stress development during the processing of thin organic films. Outside of graduate school, Jason enjoys biking, hiking (anything outdoors), weightlifting/fitness and playing the cello.

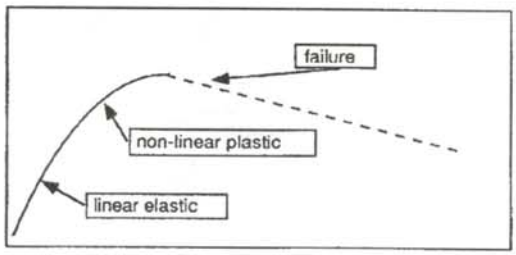

Figure 1
Representative stress-strain curve.

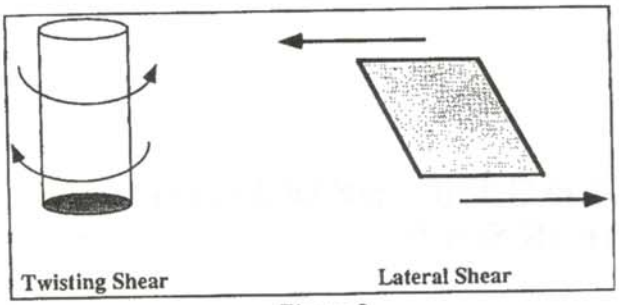

Figure 2
Two methods of exerting a shear on a solid.

of fundamental interest to materials scientists, because their properties place them at an intermediate stage between solids and liquids. Commercially available instruments are designed to study engineering materials, such as steel, and are not useful for investigating weak solids. A new technique is needed to study the shear properties of weak solids.

THE INSTRUMENT

A solid can be sheared by either twisting it or by moving two parallel faces in opposite directions as shown in Figure 2. We decided to use the twisting method to a apply the shear, using a concentric cylinder configuration. The shearing cell consists of a stationary outer cylinder and an inner cylinder attached to a precision ball bearing coupled by the material under study. A schematic diagram of the instrument is shown in Figure 3. To create the stress on the solid, a magnet was mounted on the inner cylinder and the shearing cell placed in the center of the coils of a Helmholtz pair. The interaction between the field of the Helmholtz pair and the magnet twisted the inner cylinder.

The magnetic field at the center of a Helmholtz pair is:

$$B_H = \frac{\mu_o N I}{R\left(\frac{5}{4}\right)^{\frac{3}{2}}} \qquad (2)$$

where B_H is the magnetic field (in Gauss), μ_o is the permeability of free space, I is the current passing through the coils (Amps), R is the radius of the coils (in meters) and N is the number of turns in one coil. For a Helmholtz pair, the two coils are separated by a distance equal to the coil diameter. The gradient of B_H is 0 in the region at the center of the coil pair. This means that the magnetic field of a Helmholtz pair is spatially uniform. Consequently, a small magnet placed in the field of the Helmholtz pair will experience a pure torque without being affected by any lateral forces. A computer controlled power supply was used for precise control and accurate measurement of the current flowing through the coils. This controlled the torque on the magnet and hence the shear exerted on the solid. The large current range of the supply allowed for a broad range of applied torques.

We decided to use an optical lever to measure the angular displacement of the solid. Although less precise than interferometric techniques, the optical lever allowed us to track large displacements. It also kept the instrument relatively simple and inexpensive.

RESULTS

We tested the instrument with a weak solid that was close to the liquid/solid phase boundary. We chose lemon Jello which had the properties for which we were looking. A typical data set for lemon jello is shown in Figure 4. A well defined solid-like response was indicated. The Jello supported a finite shear stress with out flowing . The stress-strain relationship is quite linear and a well defined shear modulus, G, can be extracted from the slope. It is possible that measurements over a broader range of strains will reveal more complex behavior. The uncertainty along the strain axis is due to the unfocused laser beam that was used in the optical lever.

A second test was done using agarose gel. This material is used in biology as a growth medium for bacteria. It is

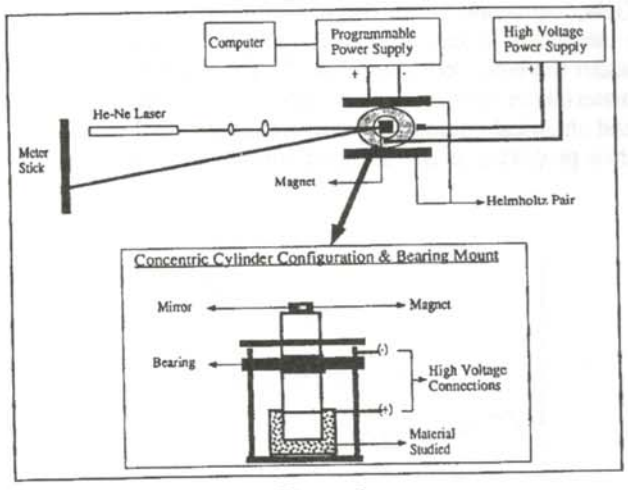

Figure 3
Schematic diagram of the instrument showing the shear cell, the Helmholtz pairs and the optical lever.

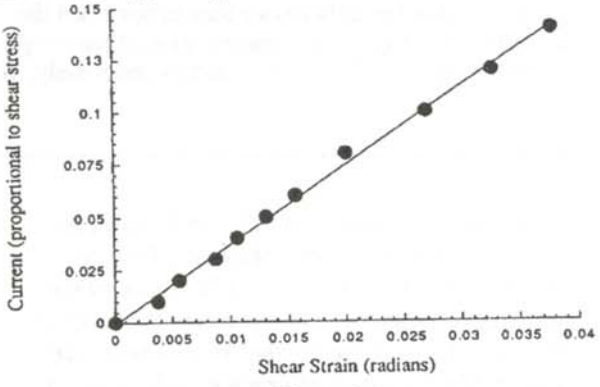

Figure 4
Results for lemon jello. The straight line indicates that there is a well defined shear modulus for this weak solid.

particularly easy to use because it is a gel at room temperature and only needs to be warmed slightly to make it a liquid again. This makes it easy to pour the material into the annular space where it is allowed to gel in place. Another feature of agarose gel is that the elastic constant of the material varies with the concentration of agarose. Typical results of these measurements are shown in Figure 5.

As the concentration of agarose increases, the slope of the (τ–γ) graph increases. This implies that the shear modulus of agarose gel increases rapidly in this range of concentrations. This qualitatively agrees with the expectation that the cross-linking density increases at the microscopic level with an increase in concentration. A detailed study of the concentration dependence of the shear modulus of agarose gel is currently in progress.

After validation with the studies discussed above, we applied the technique to a class of materials known as electrorheological fluids (ER).

These fluids are colloidal suspensions of particles of high dielectric constant, neutrally buoyant in an oil of a smaller dielectric constant. Their response to an electric field is frequently described as a very large increase in their viscosity. Recently, however, various groups have begun to describe them more in the language of solids. For example, there have been attempts to measure the yield stresses and shear moduli of these materials in the presence of an electric field. Frequently the results are not reproducible. The contemporary research community often debates if there is any yield stress at all. In deed, there are claims that these materials behave essentially like a liquid and have no yield stress, down to the smallest strain rates that have been measured.

We believe that these claims represent more of an inability to apply very small stresses and very small strain rates. As shown in Figure 6, the suspension of corn starch in mineral oil, in an electric field of 6 kV/cm, shown unambiguously

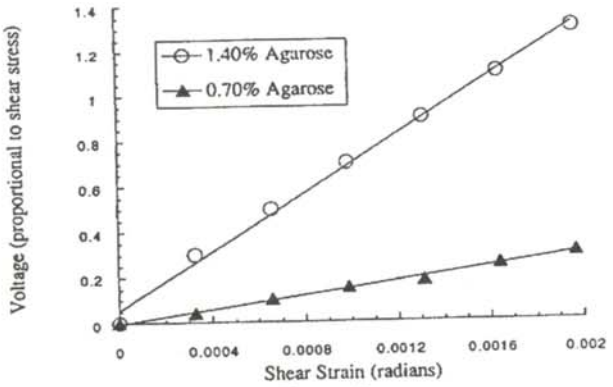

Figure 5

Results for agarose at various concentrations. The rapid increase in the shear modulus (slope of the line) in this range of concentrations shows an increase in the cross-linking density with an increase in concentration.,

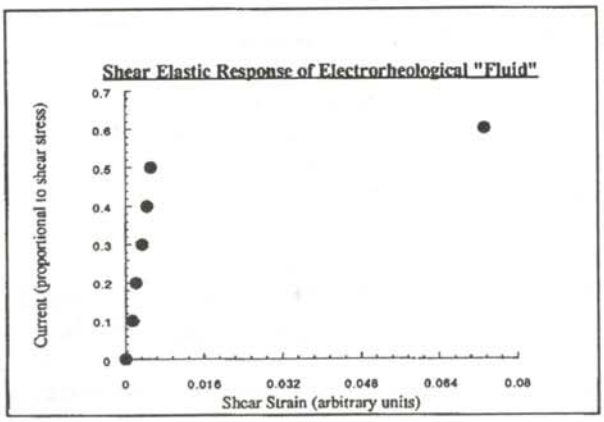

Figure 6

Response of corn starch, suspended in mineral oil, in an electric field of 6 kV/cm. This suspension is an electrorheological "fluid".

a linear, solid-like shear elastic response from which a shear modulus can be extracted. The discontinuity at and above a current of 0.5A corresponds to what one might call a yield stress. It would not have been possible to delineate this well defined solid-like behavior, including the linear regime and recoverable strain, if one could not make measurements for very small stresses and strains. In the coming months, we intend to explore the mechanical response of various ER fluids extensively using this instrument at various applied electric fields, various concentrations of suspensions.

SUMMARY

We have designed and built a simple and inexpensive instrument that can apply small stresses and measure small strains needed to study the shear elastic response of weak solids. Through the use of electromagnetic and optical tools, we have achieved sufficient precision to investigate contemporary research problems, such as electrorheological "fluids".

Plans to improve the sensitivity and accuracy of our instrument are currently being sketched out. The unfocused laser beam will be collimated in the near future. This will enable us to obtain more precise measurements of the angular displacement of the inner cylinder. Other improvements will include the use of better precision bearings, or perhaps the use of magnetically levitated bearings.

The instrument will be modified to incorporate two Helmholtz pairs at right angles to each other that are driven by sinusoidal currents that are 90 degrees out of phase with each other. This will produce a rotating magnetic field at the inner cylinder and maintain a constant shear strain on the liquid.

ACKNOWLEDGMENTS

This work was supported by a NASA/JOVE grant to the

Illinois Wesleyan University Department of Physics.

REFERENCES

* Current Address of the author: University of Minnesota, 151 Amundson Hall, 421 Washington Ave., S.E., Minneapolis, MN 55455.

1. Gast, A.P. and C.F. Zukoski, Advances in Colloid and Interface Science, 80, 1989, p. 153.
2. Sprecher, A.F., Y. Chen and H. Conrad, Proceedings of the Second International Conference on ER Fluids, Technomic Publishing, 1990, p. 82.
3. Payne, J.A. and N.K. Jaggi, Bulletin of the American Physical Society, 38, 1, 1993, p. 396.

FACULTY SPONSOR

Dr. Narendra K. Jaggi
Laboratory for Materials Physics
Illinois Wesleyan University
Bloomington, IL 61702-2902

SCANNING TUNNELING MICROSCOPY OF CYTOSINE

Debra J. Lightly*
Physics Department
Arizona State University
Tempe, AZ 85287-1504
received November 17, 1993

ABSTRACT

An electrochemical scanning tunneling microscope was used to image cytosine molecules adsorbed onto an Au(111) surface in solution. A three-electrode setup allowed the electrochemical potential to be monitored and controlled during scanning. The rest potential was positive, allowing for spontaneous adsorption. Variation of the electrochemical potential caused a change in the two-dimensional lattice structure of the adsorbed cytosine molecules.

INTRODUCTION

The scanning tunneling microscope (STM), developed by G. Binnig and H. Rohrer in the early in the 1980's, was initially used to image conducting surfaces in a vacuum.[1] In this application, the operation of the STM can be explained using the "particle-in-a-box" model. The STM tip and the conducting surface are separated by a distance d, such that a barrier of potential energy V and width d exists. There exists a probability that an electron can tunnel through this classically forbidden region because the wavefunctions of the Fermi level electrons decay exponentially through the barrier with a characteristic inverse decay length, κ:

$$\kappa = \sqrt{\frac{2m\phi}{\hbar^2}} \qquad (1)$$

where m is the mass of the electron, $\phi = V - E$ is the workfunction of the material, V is the barrier height and E is the total energy of the electron.[2] If the separation d is so small that the tip and the sample wavefunctions overlap, a transition of an electron from the tip to the sample or from the sample to the tip is possible, thus establishing a flow of electrons. This flow of electrons, I, is the tunneling current, a measure of the wavefunction overlap or the tip-sample separation, and is given by:

$$I \approx I_o e^{-2\kappa d} \qquad (2)$$

The STM tip scans the surface using piezoelectric drivers and a feedback system to keep the tunneling current constant. By recording the vertical motion of the tip relative to the sample, the surface topography is mapped.

Tunneling through other insulators, such as air and water, is also possible. In addition, tunneling can take place in an electrolytic solution. Although an electrolyte is an ionic conductor, it is an insulator with respect to electron flow.[3] In this application, ionic conduction can be minimized by insulating the scanning tip with wax. The use of a STM to image in water and solution is an important development in microscopy for biological samples, as biological molecules function only in a water environment. Tunneling is limited to metals and semiconductors. However, nonconducting molecules can be imaged if they are adsorbed onto a conductor. This adsorption is accomplished from an aqueous solution by controlling the electrochemical potential.

Electrochemical STM has been used to obtain images of DNA molecules[4] as well as molecules of the individual DNA bases (adenine, thymine, guanine and cytosine).[5] The cytosine molecules adsorb onto a gold surface in an ordered oblique lattice.[5] The lattice dimensions are a = (10.5±0.2)Å and b = (9.5±0.2)Å with γ = (102±3)°. Each

Debra J. Lightly graduated from Austin (MN) High School in 1991 and is presently a junior physics major at Gustavus Adolphus College. She is the vice-president of the GAC physics club and plays French horn in the Gustavus Band. At Gustavus, she has assisted with optical absorption research involving silicon-tellurium glasses. Her current research project at Gustavus is building a Scanning Tunneling Microscope. She plans to pursue graduate in physics or a related area.

unit cell contained a central cytosine molecule, which appeared as a bright spot, and a large black hole. The bright spot indicates that the topography is high, while low topography appears dark. Each cell shared its vertices with 4 other bright spots. The lattice was at an angle of (30±3)° with respect to the gold lattice.

Once DNA molecules can be routinely imaged at resolutions which reveal the individual bases in the molecules, sequencing the bases using STM might become possible. We are investigating the change in the two-dimensional lattice structure of the adsorbed cytosine molecules with change in electrochemical potential because this is believed to be a unique property for each of the bases.

EXPERIMENTAL METHOD

The microscope

The STM used was designed to hold the sample stage, a circular plate, beneath the scanning tip.[6] The plate was in contact with three magnetic legs, one of which was controlled by a driver, providing vertical motion of the tip relative to the plate. A glass cylinder was fitted over the plate so that the sample chamber was hermetically sealed. The chamber was then sparged with clean, humidified N_2 gas. Drift was limited to approximately 1 Å/minute. Tunneling currents on the order of picoAmps in solution were possible. The tips were made from $Pt_{0.8}Ir_{0.2}$ by an etching process,[7] and were coated with wax. They gave essentially no leakage current.

Gold substrate

The cytosine molecules were electrochemically adsorbed onto a gold substrate. The substrates were prepared under ultrahigh vacuum conditions by growing gold epitaxially on a heated mica surface.[8] Care was taken to ensure that the gold was both flat and clean, so that adsorbed molecules could be imaged. The substrates were stored in an argon atmosphere until used. They were exposed to laboratory air only for a few minutes, before being stored

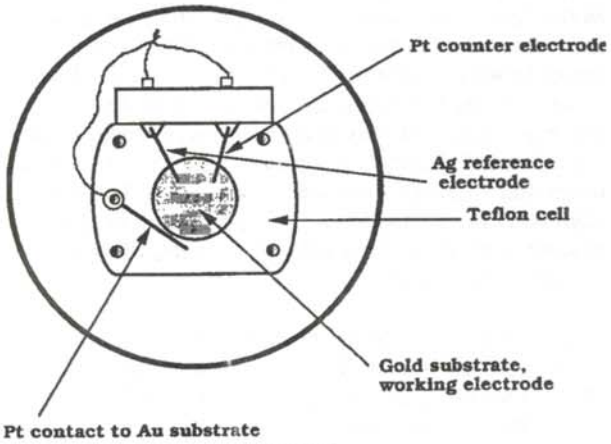

Figure 1

A top view of the circular sample stage with mounted teflon cell and working, reference and counter electrodes.

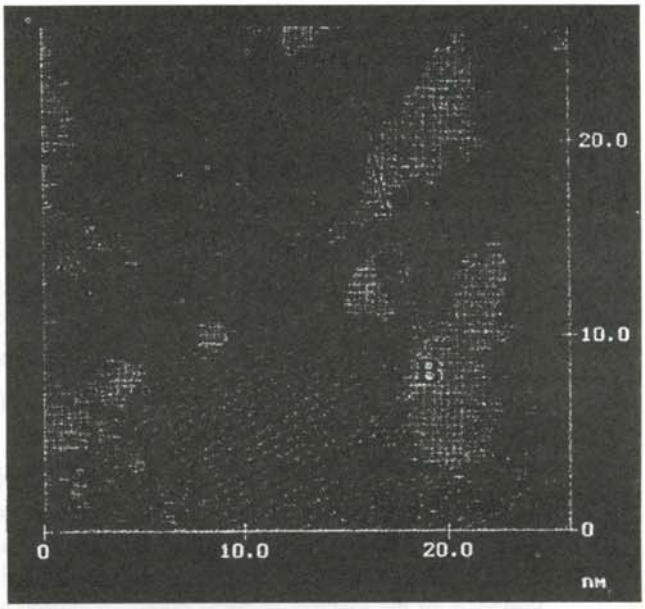

Figure 2

Cytosine molecules imaged at +50 mV after forced adsorption onto Au(111) surface. A: Lying-down structure, appearing as bright spots in rows. B: Stacked structure, worm-like rows.

and while being mounted on the STM sample stage. Very clean substrates showed Au(111) surface as a double-stripe pattern, where adjacent stripes were separated by about 70 Å (commonly seen in ultrahigh vacuum).[9]

Electrochemistry

A teflon cell, shown in Figure 1, was mounted on the STM plate with a gold substrate beneath a circular hole in the cell. The STM tip extended into this hole, which had a volume of 70 µl and contained the solution through which the tunneling occurred. Three electrodes were used: the working electrode, the reference electrode and the counter electrode. The gold substrate was the working electrode, electrical connection was made to the gold using a Pt wire. The reference electrode was an Ag wire which extended into the solution. This electrode was necessary because absolute potentials cannot be measured. The counter electrode, a Pt wire extending into the solution, kept the potential difference between the gold substrate and the reference electrode constant. The electrochemical potential that was of interest to our research was the potential between the working electrode (gold substrate) and the Ag reference electrode. The electrolyte used was a 100 mM $NaClO_4$ solution made with 18 MΩ purified water. 20 µl of a 10 mM cytosine solution were added with 50 µl of the electrolyte. The cell and electrodes were freshly prepared for each run to prevent the gold substrate from becoming contaminated.

Imaging and resolution

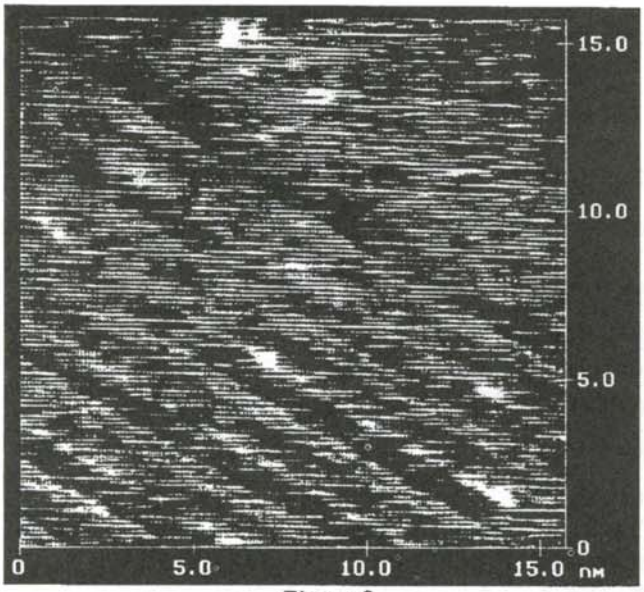

Figure 3

Cytosine molecules spontaneously adsorbed and imaged at the rest potential. Alternating rows of high and low contrast, with high-contrast rows appearing as double stripes.

When possible, the initial imaging for each run was carried out before the cytosine molecules were adsorbed onto the surface. The measured rest potentials for such runs were on the order of -50 mV with respect to the gold. A slightly positive rest potential, on the order of 30 mV, permitted spontaneous adsorption of the cytosine molecules, preventing imaging prior to adsorption. The tunneling current used ranged from 0.10 nA to 0.30 nA. The tip bias was set to 100 mV. The resolution varied from run to run as well as during individual runs because the resolution was dependent on the state of the STM tip, which continually changed. Very good resolution resulted from a geometry where a single atom or a few atoms were at the end of the tip.

RESULTS AND ANALYSIS

Figure 2 shows a typical scan. Two different structures were seen, a stacked structure and a lying-down structure. Both structures were often seen in the same image. We could observe the domain boundaries.

The lying-down structure, shown at A in Figure 2, was a planar structure which appeared as bright spots in rows, with very little dark space between the rows. With slightly less resolution, the individual molecules could not be seen, but the rows were still visible. The row separation was measured to be (6.3±0.3)Å. The separation of the molecules within each row was (5.2±0.3)Å. The molecules in adjacent rows were shifted such that an angle of (110±3)° was formed between a row and a line connecting nearest neighbor molecules in adjacent rows.

The rows of the stacked structure, shown at B in Figure 2, appeared worm-like and narrow, leaving more dark space between the rows than seen for the lying-down structure. The spacing of the rows was measured to be (4.9±0.3)Å. Intra-row spacing was difficult to measure quantitatively, but the stacked molecules were more closely packed than the lying-down molecules.

Variation of the electrochemical potential between +300 mV and -140 mV after the forced adsorption at +50 mV produced no change in the two-dimensional lattice structure of the cytosine molecules. The molecules remained adsorbed onto the surface of the gold substrate.

Spontaneous adsorption of the cytosine molecules at a positive rest potential produced a lattice structure consisting of rows of alternating high and low contrast as seen in Figure 3. The orientation of the molecules in the high-contrast rows was such that a single row of molecules appeared as a double stripe. The separation between high contrast rows was measured to be (12.3±0.3)Å.

Variation of the electrochemical potential from rest potential to +250 mV after spontaneous adsorption produced a change in the two-dimensional lattice structure of the molecules. The alternating rows of high and low contrast were still intact at +150 mV. By +200 mV, however, this structure was replaced by bright spots in slightly disordered rows as shown in Figure 4. The spacing between rows was measured to be (4.9±0.5)Å. This structure remained unchanged at +250 mV.

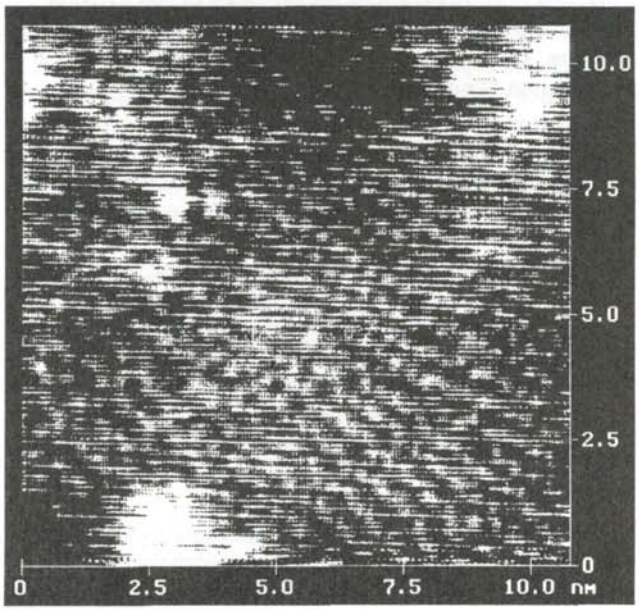

Figure 4

Spontaneously adsorbed cytosine molecules imaged at +200 mV after an electrochemically driven change in the two dimensional lattice structure. Bright spots (molecules) in slightly disordered rows of equal contrast.

INTERPRETATION OF RESULTS

A change in the lattice structure was observed only when the cytosine molecules could adsorb spontaneously. In this case, the interaction between the cytosine molecules was greater than the interaction between gold and cytosine. This caused a sheet of cytosine molecules to form, which "floated" above the gold surface. The intermolecular interactions permitted two different molecular orientations: a low-contrast row and a double-striped, high-contrast row. As the electrochemical potential was increased, the interaction between gold and cytosine became stronger. By +200 mV it exceeded the intermolecular interaction. This caused the sheet of alternating rows of high and low contrast to disappear and be replaced by a structure appearing as bright spots in rows of equal contrast, indicating a single molecular orientation.

The rest potential, which could not be controlled, was often negative, preventing spontaneous adsorption. When we forced the gold to be positive, the gold-cytosine interaction was made to exceed the cytosine-cytosine interaction and the "floating sheet" was never formed. Each cytosine molecule was adsorbed onto a particular spot on the gold surface, forming either a lying-down or stacked structure. Increasing the electrochemical potential simply increased or decreased the strength of the adsorption, but did not change the orientation or two-dimensional lattice of the molecules.

ACKNOWLEDGMENTS

The author thanks S.M. Lindsay for his guidance and J. Pan and T.W. Jing for their laboratory assistance. This work was performed under the auspices of the Arizona State University Physics Research for Undergraduates Program, supported by the National Science Foundation and Arizona State University.

REFERENCES

* Present address of the author: Gustavus Adolphus College, St. Peter, MN 56082.

1. Binnig, G. and H. Rohrer, Rev. Mod. Phys., 59, (1987), p. 615.
2. Zangwill, A., Physics at Surfaces, Cambridge University Press, (1988).
3. Sonnenfield, R., J. Schnier and P.K. Hansma, in Modern Aspects of Electrochemistry, ed. by R.E. White, J. O'M. Bockris and B.E. Conway, Plenum Publishing Corp., (1990).
4. Lindsay, S.M., T. Thundat, L. Nagahara, U. Knipping and R.L. Rill, Science, 244, (1989), p. 1063.
5. Tao, N.J., J.A. DeRose and S.M. Lindsay, J. Physical Chem., 97, (1993), p. 910.
6. Jing, T.W. *et al.*, in press.
7. Nagahara, L.A., T. Thundat and S.M. Lindsay, Rev. Sci. Instrum., 60, (1989), p. 3128.
8. DeRose, J.A., T. Thundat, L.A. Nagahara and S.M. Lindsay, Surf. Sci. 256, (1991), p. 102.
9. Tao, N.J. and S.M. Lindsay, J. Appl. Phys., 70, (1991), p. 5141.

FACULTY SPONSOR

Dr. Stuart M. Lindsay
Department of Physics and Astronomy
Arizona State University
Tempe, AZ, 85287-1504
lindsay@physast.la.asu.edu

PHASE DIAGRAMS AND LATTICE CONSTANTS OF $Si_{1-x}C_x$ RANDOM ALLOYS AND $Si_{1-x-y}Ge_yC_x$ LAYERED CRYSTALS

David H. Whysong*
Department of Physics and Astronomy
Arizona State University
Tempe, AZ 85287-1504
received December 6, 1993

ABSTRACT

Molecular dynamics simulations based on valence force fields were used to determine the cubic lattice constant and formation temperature of randomly alloyed fcc $Si_{1-x}C_x$. Similar techniques were used to determine the lattice constant and crystalline structure of an ordered structure of $Si_4Ge_3C_1$. A comparison was made between the lattice constants found for randomly alloyed silicon carbon, previous results and Vegard's law. This comparison showed that Vegard's law consistently over estimated the lattice constant of a random alloy.

INTRODUCTION

The band gap of a semiconductor is central in determining its electronic properties. Thus, the ability to create substances with varying band gaps is desirable. Silicon, one of the most widely used semiconducting materials, has a band gap of approximately 1.17eV. It is thought that alloying silicon and carbon (which has a large band gap ≈ 5.5eV) would increase the energy gap in the alloy. Optical technologies would benefit from a band gap larger than that of silicon. Semiconducting devices only require materials of different band gaps.

In the case of silicon and carbon (diamond), a large lattice mismatch of 1.86Å, nearly 34%, introduces enormous strain energies in substitutional defects of about 1.6 eV/atom [1]. Also, carbon is relatively insoluble in silicon, even at high temperatures (10^{-3} to 10^{-4} atomic percent at 1200C to 1400C).[2] However, the formation of $Si_{1-x}C_x$ with $x \approx 3.5$ atomic percent has been demonstrated [3], although some precipitation of SiC seems likely due to the unusually high lattice constant of 5.426Å. This measure lattice constant is 0.06Å greater than that suggested by Vegard's law.

David Whysong is an undergraduate physics student at Harvey Mudd College. His academic interests include computational and theoretical modelling of various physical systems. Other interests include philosophy and music. He enjoys playing the piano and the saxophone.

Vegard's law is a simple linear approximation for the lattice constant of a random alloy. In this case, the known lattice constants of pure silicon and carbon are used to define a line from which the lattice constants of random alloys may be calculated.

To produce a useful alloy, one needs two lattice compatible materials with different energy gaps. Growing the alloy on a silicon substrate requires that the alloy have a lattice constant compatible with that of silicon. Thus, a three atom alloy, $Si_{1-x-y}Ge_yC_x$ was introduced. The inclusion of germanium, which has a lattice constant slightly greater than that of silicon, a = 5.6Å, may cause a reduction in the crystal strain and allow greater carbon concentrations.

The introduction of germanium may be necessary for tuning the electronic structure as well as assisting in a lattice match with silicon. Theoretical results have shown a marked decrease in the energy gap when carbon is added to silicon in a random alloy[4]. At concentrations of about 10% carbon, the band gap may become negative, the crystal would become a conductor rather than a semiconductor.

Molecular dynamics simulations model the motion of atoms. An interaction potential between atoms of a random alloy was differentiated to obtain the forces acting on each atom. The motion of the individual atoms may then be modeled. For this work, a solution theory was used to obtain the total energy in supercell alloys.

Molecular dynamic methods, suggested by Keating, were used which employed the valence force field model to

relax a supercell of 8, 64 or 512 atoms. [5] The dynamic calculations used a fifth order Gear algorithm to calculate precise forces and positions. [6] The Keating potential involves the summation of strain energy, which is the difference between the equilibrium bond energy E_b and the actual bond energy. The strain energy associated with an atom is given by:

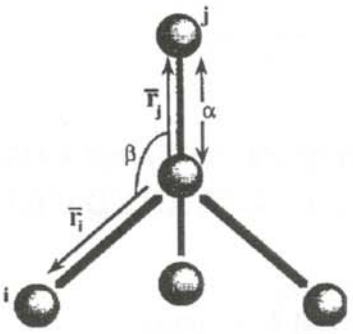

Figure 1
Variables in the Keating model.

$$U = \frac{3}{4 d_o^2}\left[\frac{1}{2}\sum_{i=1}^{4}\alpha_i \Delta(\vec{r}_i \cdot \vec{r}_i)^2 + \sum_{i,j>i}\beta_{ij}\Delta(\vec{r}_i \cdot \vec{r}_j)^2\right], \quad (1)$$

where α and β are interatomic force constant, $\vec{r}$ is the bond vector and d_o is the equilibrium bond distance. The parameters are diagrammed in Figure 1. Note that there are two significant terms; the first concerns bond length differences and the second concerns angular variation between two bonds. The $\Delta(\vec{r}_i \cdot \vec{r}_i)^2$ term represents the square of the differences between the squares of the actual bond length and the ideal bond length. This is summed over all the bonds labeled by *i*. The angular term, $\Delta(\vec{r}_i \cdot \vec{r}_j)^2$ has a dot product between two different bond vectors, giving the energy involved in altering the angle between the two bonds. The constants which were used in the calculation are shown in Table 1.

Phase Diagram

To find the temperature at which a silicon-carbon random alloy will form, the free energy, G, of the crystal must be calculated:

$$G = U - TS + PV \quad (2)$$

	α	β	d_o(Å)	E_b(eV)
Si	48.50	13.81	2.35	2.32
C	129.33	84.76	1.56	3.68
Ge	38.67	11.35	2.42	2.56
SiC	97.42	52.61	1.89	3.17
SiGe	43.59	12.58	2.39	2.73
GeC	84.00	48.06	1.94	2.59

Table 1
Constants used in the molecular dynamics simulations.

where U is the internal energy, T is the absolute temperature, S is the entropy, P is pressure and V is the volume. The internal energy is determined by molecular dynamics simulations using the Keating potential. The pressure is assumed to be zero when the lattice constant is ideal, hence the PV term is 0. The entropy is found statistically using the Boltzman equation:

$$TS = NkT[x \ln x + (1-x)\ln(1-x)], \quad (3)$$

where x is the concentration of carbon in the silicon carbon random alloy and k is the Boltzman constant.

Lattice Constant

Molecular dynamics simulations require a knowledge of the lattice constant at various concentrations. Even a slight variation in the lattice constant can cause significant extra strain in the crystal. Two theoretical techniques were used to find the lattice constant, Vegard's law and minimum energy curves. Experimental results can also provide lattice constants for some materials.

If the two elements are silicon and carbon, Vegard's law provides a simple linear expression for the alloy lattice constant A:

$$A = a_{Si}(1-x) + a_C(x) \quad (4)$$

For $Si_{1-x-y}Ge_yC_x$ alloys, Vegard's rule becomes:

$$A = a_{Si}(1-x-y) + a_{Ge}(y) + a_C(x) \quad (5)$$

where a_{Ge}, a_{Si}, and a_C are the lattice constants for germanium, silicon and carbon respectively. This forbids nonlinear variation of the lattice constant at different concentrations. Experimental results are desirable, and in

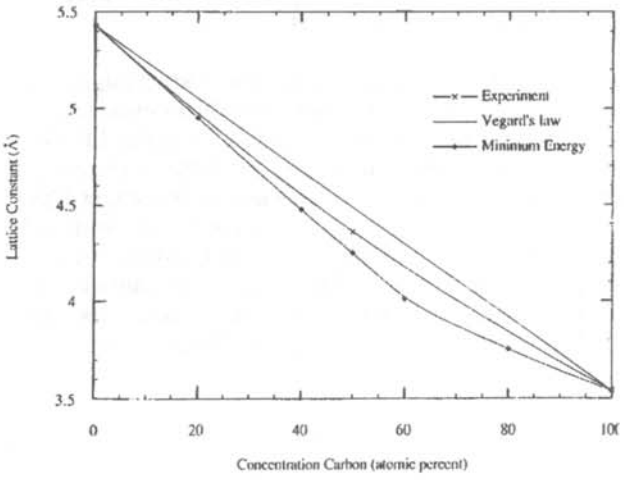

Figure 2
Lattice constant of $Si_{1-x}C_x$: Vegard's law, experimental results and minimum energy curve. The experimental result points are for silicon, carbon and silicon carbide crystals. The minimum energy results consist of silicon carbon random alloys.

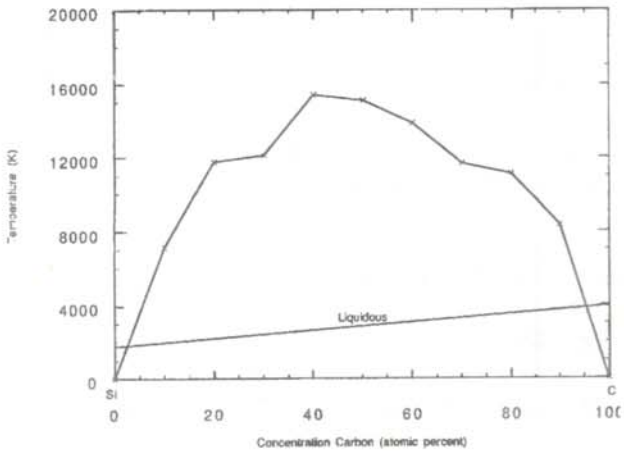

Figure 3

Phase diagram of $Si_{1-x}C_x$ random alloy as calculated from the results of 64 atom supercell molecular dynamics.

the case of silicon carbide, differ significantly from the value obtained by Vegard's law.

If the lattice constant of a crystal is forced to a non-ideal constant value, some extra strain energy will be introduced, due to pressure applied to the system. Comparing the strain energy to the lattice constant produces a parabolic arc for small changes in the alloy lattice constant. The most desirable lattice constant for a crystal of that composition must be at the minimum energy configuration, or the minimum of the strain energy vs lattice constant curve. We used this method to determine the lattice constants used in the molecular dynamics simulations. This approach was used because it is a consistent method in that the strain energy can be determined by the Keating potential, thus the minimum point will always be the best lattice constant for the molecular dynamics

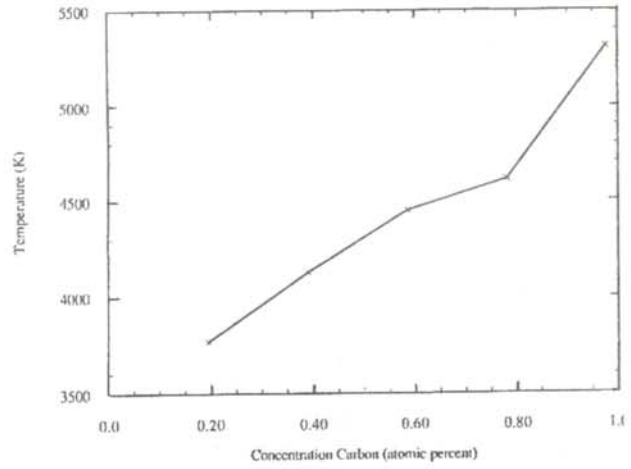

Figure 4

Phase diagram of $Si_{1-x}C_x$ random alloy calculated from the results of 512 atom super cell molecular dynamics.

simulation at that concentration.

DISCUSSION

The simulated $Si_{1-x}C_x$ random alloys displayed a tendency to disassociate bonds beyond the 2.5 Å limit imposed by the simulation. Increasing this limit to 2.6 Å was required for $x = 0.1$ and an increase to 2.7 Å was required for the simulation at $x = 0.2$. This unusually high atomic displacement indicates a tremendous strain in the crystal. It is likely that at concentrations above 2 to 3 atomic percent, the crystal will not form as a random alloy, but silicon carbide will precipitate from the pure silicon.

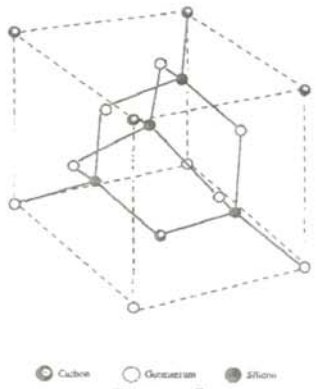

Figure 5

Layered $Si_4Ge_3C_1$ eight-atom cell.

Figure 2 shows the results for the lattice constant calculation. The graph shows a comparison with Vegard's rule and a smooth curve fit to the three known data points. There is a pronounced overestimation of the lattice constant by Vegard's equation. This may be due to the larger interatomic force constant, α, in carbons, which would cause the lattice constant to shift more towards that of carbon, even for small concentrations.

The phase diagrams shown in Figures 3 and 4 indicate temperature at which the silicon carbon random alloy may form in a zincblende lattice (face centered cubic). The line of liquidous is assumed to be linear between the melting points of silicon and carbon. The high temperatures across most concentrations indicate that when forming a random alloy at concentrations greater than a few percent, the energy required to overcome the strain is sufficient to cause precipitation of silicon carbide. Any random alloys with more than a trace of carbon will most likely either precipitate silicon carbide or form in a metastable state. This agrees with the experimental problems of producing alloys at more than a few percent carbon which have not precipitated into silicon carbide.

A series of strain energy computations were carried out for a layered form of $Si_4Ge_3C_1$ to determine the lattice parameters for molecular dynamics simulation. The structure of the cell is shown in Figure 5. The calculated strain energy as a function of lattice constant are shown in Figures 6-9. The strain energy vs. antiplanar lattice constant plots are useful in determining how large the supercell should be in a molecular dynamics simulation. By measuring the strain energy in simulations with various lattice constants, and fitting a parabolic curve to the

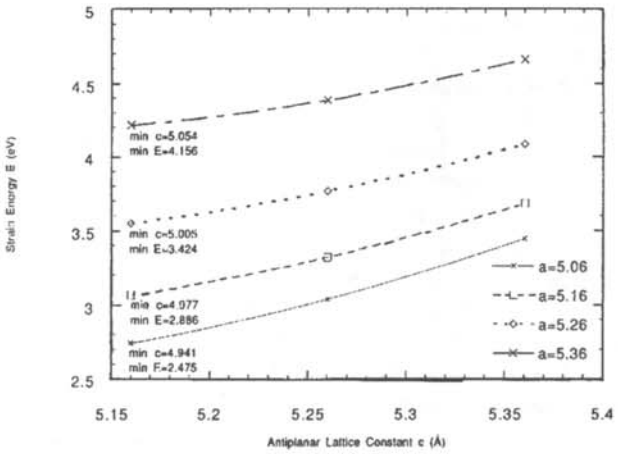

Figure 6

Layered $Si_4Ge_3C_1$ strain energy vs antiplanar lattice constant for four different different planar lattices.

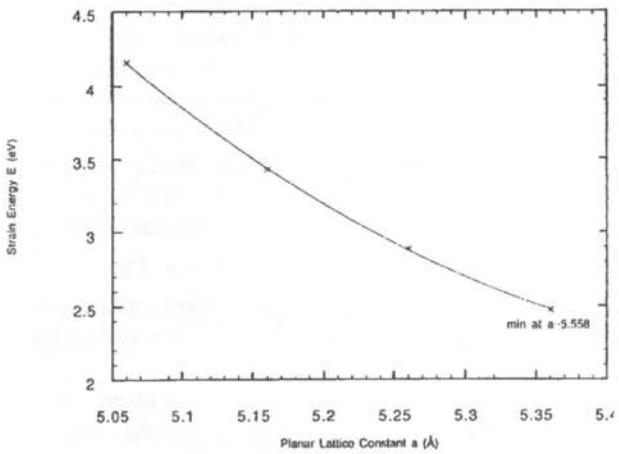

Figure 8

Layered $Si_4Ge_3C_1$ strain energy vs planar lattice parameter. The minimum of this curve marks the relaxed state.

results, a minimum strain energy configuration can be found. This is the lattice constant which is used in subsequent simulations.

Due to the planar layered structure, the anitplanar lattice constant is different from the planar lattice constant. At this concentration, Vegard's rule predicts a cubic lattice with constant of 5.26 Å. We found that the lattice is tetragonal with $a = b = 4.889$ Å and $c = 5.558$ Å. Subsequent molecular dynamics simulations in cubic cells revealed a shift in the atomic spacing between the layers such that the distance between the carbon-germanium and the silicon layers above and below decreased, while the distance between the pure germanium layer and the silicon layers increased. This may be explained by examining the equilibrium bond distances and α parameters for carbon and germanium. The carbon atom, with a greater α, exerts a greater attractive force on the nearest neighbor silicon atoms than does the germanium. At these lattice parameters, the germanium-silicon bonds are nearly relaxed, while the carbon-silicon bonds are stretched.

It is unlikely that silicon carbon random alloys will be constructed at carbon concentrations much greater than the 3.5% already found. Silicon germanium carbon alloys, such as the one simulated here, may yield reduced strain energies.

ACKNOWLEDGMENTS

Thanks are due to Otto F. Sankey and Alex Demkov for their direction and assistance. This work was performed under the auspices of the Arizona State University Physics

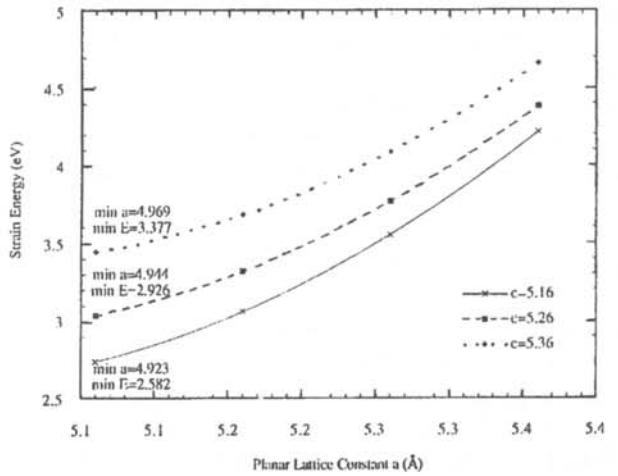

Figure 7

Layered $Si_4Ge_3C_1$ strain energy vs planar lattice constant for three different antiplanar lattices.

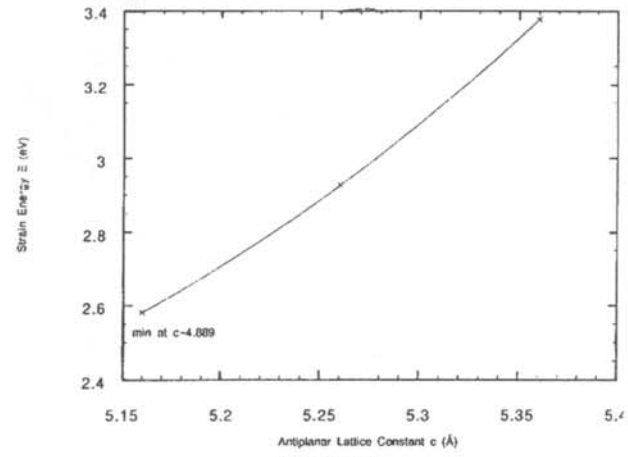

Figure 9

Layered $Si_4Ge_3C_1$ strain energy vs antiplanar lattice parameter. The minimum of this curve marks the relaxed state.

Research Experience for Undergraduates Program, supported by the National Science Foundation and Arizona State University.

REFERENCES

* Present address of author: Physics Department, Harvey Mudd College, Clarement, CA 91711.
1. J. Tersoff, Phys. Rev. Let., 64, (1990), p. 1757.
2. R.W. Olesinski and G.J. Abbaschian, Bull. Alloy. Phase Diagrams, 5, (1984), p. 589.
3. J.B. Posthill, *et al.*, Appl. Phys. Lett., 56, (1990), p. 734.
4. A.A. Demkov and O.F. Sankey, to be published in Phys. Rev. B.
5. R.M. Martin, Phys. Rev. B., 1, (1970), p. 4005.
6. M.P. Allen and D.J. Tildesley, Computer Simulation of Liquids, Oxford: Clarendon Press, (1987).

FACULTY SPONSOR

Dr. Otto Sankey
Department of Physics and Astronomy
Arizona State University
Tempe, AZ 85287-1504
sandey@edison.la.asu.edu

THE CONSTRUCTION AND OPERATION OF A CsI DETECTOR ARRAY FOR THE BGO BALL AT LAMPF

Eric V. Beck* and James C. Beck **
Physics Department
Arizona State University
Tempe, AZ 85287-1504
received October 1, 1992

ABSTRACT

A 9-element CsI calorimeter detector array was built to close the beam exit hole of the BGO Ball 4π detector at LAMPF. The array can serve as a calorimeter for protons and pions with energies up to 260 MeV and 160 MeV respectively. The construction of the calorimeter and its performance during initial operation at LAMPF are discussed.

INTRODUCTION

Large solid angle detectors are of importance in nuclear physics when measuring total cross sections directly. They reduce the need to extrapolate from differential cross sections at unmeasured angles. Detectors used in many nuclear physics experiments subtend a solid angle on the order of 10^{-2} steradians. The detector is moved to different angles with respect to a fixed target to measure differential cross sections. If the reaction being studied involves a two body final state, the detection of one particle makes the reconstruction of the path of the other particle possible. Three-body final states require the detection of two particles to perform the same kinematic reconstruction. The measurement of a total cross section requires the ability to detect all possible final states and, therefore, all trajectories. This is best accomplished if the target is completely surrounded with detection equipment, covering all 4π of the available solid angle.

The BGO Ball is such a detector that is used in nuclear physics experiments at the Clinton P. Anderson Meson Physics Facility (LAMPF). To cover a large solid angle, the ball consists of 30 bismuth germinate (BGO) detectors that form a truncated icosahedron, with two pentagons removed to allow for beam entry and exit. In this configuration, the BGO ball covers 30/32 of the laboratory solid angle. More detailed information on the BGO large solid angle detector is available elsewhere.[1]

A 9-element CsI calorimeter was added to the BGO ball for several reasons:

a) to close the downstream hole in the detector, where

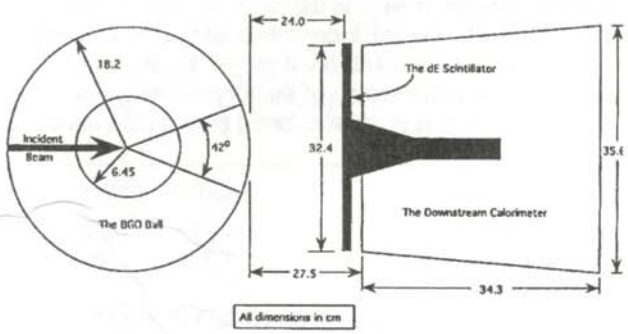

Figure 1
The relative positioning of the downstream array and the ΔE counter with respect to the BGO ball.

James C. Beck received his B.S. in physics from Arizona State University in May 1992. He is currently pursuing a Ph.D. in physics at the University of Washington in Seattle. In his spare time, James plays timpani in the university orchestra and drinks entirely too much coffee.

Eric V. Beck graduated from the University of Nevada-Reno with a B.S. in Physics and Mathematics in May of 1993. He is currently employed as a seismic technician in the Seismological Laboratory at the University of Nevada-Reno. He used to spend his free time fiddling with computers, but now is busy keeping his new baby out of the cabinets

The two authors are not related. It is just a quirk of fate that they have the same last name.

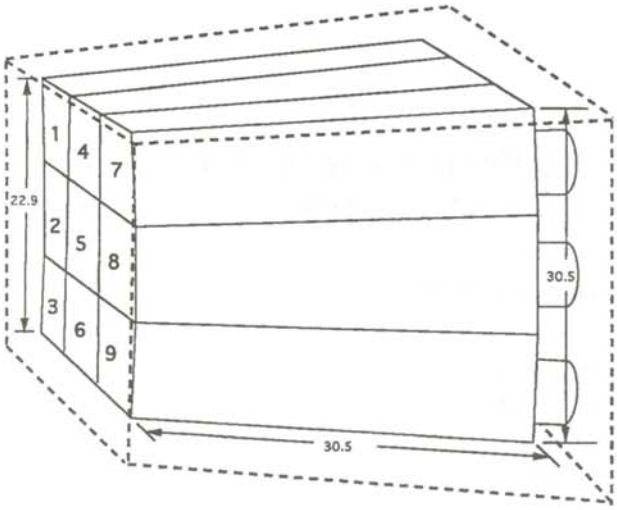

Figure 2
Schematic diagram of the downstream array (dimensions in cm).

fixed-target kinematics compress scattering events in the forward direction
b) to provide the same approximate θ and ϕ information as the BGO ball
c) to serve as a veto to reject unscattered incident particles
d) to allow for particle identification on a plot of total energy, E, versus differential energy loss, ΔE.

The relative positions of the BGO ball, the downstream calorimeter and the plastic ΔE scintillator are shown schematically in Figure 1.

THE CALORIMETER

The most important element of this detector array is the CsI scintillator whose properties are listed in Table 1. Pure CsI has an emission spectrum with a fast component at 330 nm and a slow component at 450 nm.[3] We detected the fast pulse, since its wavelength is within the sensitivity range of our photomultiplier tubes (PMT) and the light output of the fast component is high. The high density of the crystal stops the very energetic particles produced in nuclear reactions as well as the particles from the primary beam. The 30.5 cm thick crystals could completely stop 260 MeV protons and 160 MeV pions. Because this particle detector absorbs all of the kinetic energy of the incident particles, it is often referred to as a calorimeter.

Property	CsI	Plastic
Density (g/cm^3)	4.51	1.032
Index of Refraction	1.788	1.58
Decay constant (ns)	25	2
Max. Emission Wavelength (nm)	300	425

Table 1
Properties of the scintillation materials.[2]

The face of each crystal was 7.6 cm x 7.6 cm, tapering along its 30.5 cm length to a 10.2 cm x 10.2cm square. The end of the crystal was coupled to a Hamamatsu R4017 PMT with an optical cement.

A large area plastic scintillator was used as a ΔE detector. The 9.5 mm thick, 48.3 cm long and 30.5 cm wide scintillator covered the entire face of the calorimeter. The characteristics of the plastic scintillator are also shown in Table 1. Lucite light guides, attached to the left and right ends of the scintillator, wrapped around the calorimeter box and were fixed to PMT's with optical grease. The use of two PMT's allowed us to determine the geometric average ΔE pulse height, providing a more accurate energy loss measurement and reducing the position sensitivity.

An aluminum box, shown in Figure 2, was constructed to hold the crystal assembly. The light guides of the crystals were fed through holes in the back of the box. The crystals were held in place with thin pusher plates so that the calorimeter box could be rotated to access the crystal light guides without the crystals slipping out of the box. The entrance window of the box was made of 38.1μm thick tevlar, a thin, black, light tight plastic material. Each PMT was covered with a μ-metal hood which shielded from stray magnetic fields from the accelerator magnets. The μ-metal hoods were then sealed to the box and made light tight using O-rings.

OPERATION

Initial Testing
After testing for light leaks, and before moving the array to the LAMPF LEP (low energy pion) channel, a high voltage was applied to each PMT and the mean pulse height was recorded to allow for gain matching during the experimental setup. The energy resolution of each crystal was also measured. A ^{60}Co source was placed at the entrance window near the crystal being tested. The source was then removed and a background spectrum subtracted for the same length of time. The 1.33 MeV photopeak was located and fit to a Gaussian function. The resolution was calculated by dividing the full width at half maximum by the centroid of the peak. A typical pulse height resolution for the CsI crystals was 25%.

Experimental Setup and Calibration
The calorimeter was moved to the LEP channel and positioned 24 cm behind the BGO ball. This distance maximized the projected area of the ball's exit pentagon onto the face of the array. The ΔE counter was positioned directly in front of the calorimeter. Raw signals from the PMT's were sent to analog-to-digital converters (ADC) which sent signals via CAMAC equipment to a MicroVAX computer. The pulse height of the signal is proportional to the energy deposited by the particle. Multiplying that number by some known calibration parameter yields the energy of the detected particle.

The calorimeter was calibrated by directing a 50 MeV pion beam on each crystal and adjusting the PMT voltage until the pion yield of all tubes matched each other. The individual pulses from the CsI and plastic scintillators were recorded with a fast oscilloscope. The measured decay constant for the CsI crystals of 25±3 ns is consistent with the published values.

To eliminate background events and to verify that the calorimeter was detecting scattered particles, a scattering event was required to pass a series of logical tests. In incoming pion has to pass through a hole in a scintillator upstream of the BGO ball, then through a thin scintillator placed next to the target. An unscattered pion should enter the center crystal of the calorimeter, so an anti-coincidence with the center crystal was required. Finally, since this experiment was looking for a two or more body final state, two hits in the BGO ball and calorimeter were required for an event to be considered valid.

We also measured the time-of-flight of the scattered particles. A signal in the scintillator next to the target started the time-to-digital-converter (TDC). A signal from a crystal in the calorimeter stopped the TDC timer. This time was converted into a number which is related to the speed of the scattered particle.

RESULTS

The performance of the calorimeter was evaluated by scattering 90 MeV and 135 MeV pions from a CD_2 target. We expect to see scattered protons from $d(\pi,p)p$ and $^{12}C(\pi,2p)$ reactions and pions from elastic scattering from carbon and deuterium. For each scattering event, the ADC and TDC numbers were placed into histograms that allowed for visual inspection of the data and the rejection of bad events. In the histogram of the TDC spectrum, two peaks are apparent: a large peak at $t = 0$ corresponding to accidental triggering of the TDC, and a second peak at a later time that corresponds to true scattering from the tartet. Using the data from this histogram, an additional restriction of good time of flight was added to the criterion for a valid event.

The calorimeter and the ΔE counter in unison can be used to identify particles. The energy deposited by a particle in a thin scintillator is directly proportional to both the mass and the transit time of the particle. This means that a proton of a certain energy will deposit more energy in the ΔE counter than a pion of the same energy. Therefore, a histogram of the energy deposited in the CsI crystal versus the energy deposited in the E counter should show the different mass particles in continuous bands

A histogram of E vs ΔE for a 90 MeV pion beam on a CD_2 target for events that passed all tests is shown in Figure 3. Protons form the upper curved band while pion scattering events form the smaller band below it. Since the proton is roughly seven time more massive than the pion, these

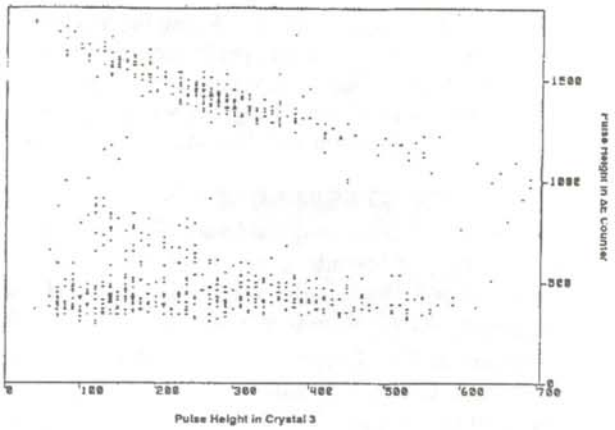

Figure 3
E vs ΔE spectrum for 90 MeV pions incident on a CD_2 target.

bands are easily resolved. Separation of more equally mass pions and muons was not always possible with this calorimeter. The muons are located on the left side of the lower horizontal band, but do somewhat overlap the pion band. Neutral particles that deposit little energy in the ΔE counter and nearly all their energy in the CsI crystal are also located in this horizontal band, worsening the pion-muon resolution. Figure 4 shows a similar histogram for a beam energy of 135 MeV pions. In experiments where separation of protons is important, the calorimeter performs well.

ACKNOWLEDGMENTS

The authors wish to thank Professor Barry Ritchie for his guidance and help in preparing this paper. They also wish to thank Doug Watson, Chris Morris, Mohini Rawool-Sullivan, Issac Cordova and Lee Atencio for providing

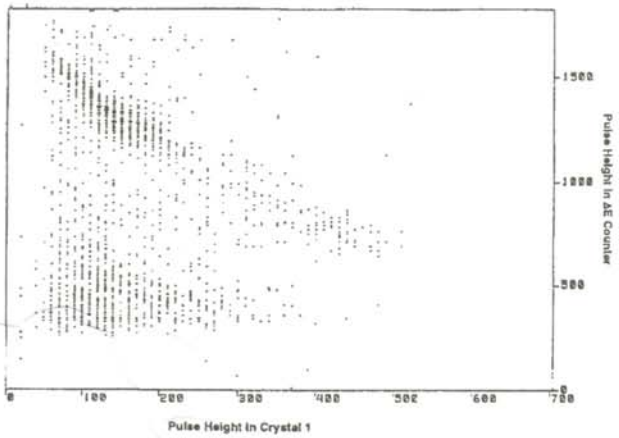

Figure 4
E vs ΔE spectra for 135 MeV pions incident on a CD_2 target.

information and technical assistance during the assembly of the calorimeter. This work was performed under the auspices of the Arizona State University Physics Research Experience for Undergraduates Program, sponsored by the National Science Foundation and Arizona State University.

REFERENCES

* Present address: Seismological Laboratory, Mail Stop 174, University of Nevada-Reno, Reno, NV 89557.
** Present address: Department of Physics, University of Washington, FM-15, Seattle, WA 98195.
1. R.D. Ransome, V.R. Cupps, S. Dawson, R.W. Fergerson, A. Green, C.L. Morris, J.A. McGill, J.R. Comfort, B.G. Ritchie, J.R. Tinsley, J.D. Zumbro, R.A. Loveman, P.C. Gugelot, D.L. Watson and C.F. Moore, Phys. Rev. C42, (1990), p. 1500.
2. W.R. Leo, Techniques of Nuclear and Particle Physics Experiments, Springer-Verlag, (1987)
3. P. Schotanus, IEEE Trans. on Nucl. Sci., 37, (1990), p. 177.

FACULTY SPONSOR

Dr. Barry G. Ritchie
Department of Physics and Astronomy
Arizona State University
Tempe, AZ 85287-1504
Ritchie@phyast.la.asu.edu

The Journal of Undergraduate Research in Physics

The Journal of Undergraduate Research in Physics is the journal of Sigma Pi Sigma and the Society of Physics Students. It is published by the Physics Department of Guilford College, Greensboro NC 27410. Inquiries about the journal should be sent to the editorial office.

The Journal of Undergraduate Research in Physics

Editorial Office -
The Journal of Undergraduate Research in Physics
Physics Department
Guilford College
Greensboro, NC 27410
910-316-2279 (voice)
910-316-2951 (FAX)

Editor -
Dr. Rexford E. Adelberger
Professor of Physics
Physics Department
Guilford College
Greensboro, NC 27410
ADELBERGERRE@RASCAL.GUILFORD.EDU

The Society of Physics Students

National Office -
Dr. Donald Kirwin, Executive Director
Ms. Sonja Lopez, SPS Supervisor
Society of Physics Students
American Institute of Physics
1 Physics Ellipse
College Park, MD 20740
301-209-3007

President of the Society -
Dr. Fred Domann
Department of Physics
University of Wisconsin at Platteville

President of Sigma Pi Sigma -
Dr. Reuben James
Department of Physics
SUNY College at Oneonta